


An anticoagulant supercapacitor for implantable applications

Received: 18 August 2023

Accepted: 22 November 2024

Published online: 03 December 2024

 Check for updates

Xiangya Wang, Meimei Yu, Mohammed Kamal Hadi, Jianzhou Niu, Yuxia Zhang, Qi Zhou & Fen Ran  

With the rapid advancement of implantable electronic medical devices, implantable supercapacitors have emerged as popular energy storage devices. However, supercapacitors inevitably come into direct contact with blood when implanted, potentially causing adverse clinical reactions such as coagulation and thrombosis, impairing the performance of implanted energy storage devices, and posing a serious threat to human health. Therefore, this work aims to design an anticoagulant supercapacitor by heparin doped poly(3, 4-ethylenedioxythiophene) (PEDOT) for possible applications in implantable bioelectronics. Heparin (Hep), the as-known anticoagulant macromolecule acts as the counterion for PEDOT doping to enhance its conductivity, and the bioelectrode material PEDOT: Hep with anticoagulant activity is synthesized via chemical oxidation polymerization. Concurrently, the anticoagulant supercapacitor is constructed through in-situ polymerization, where PEDOT: Hep and bacterial cellulose as electrode material and electrolyte layer, respectively. Owing to the incorporation of heparin, the supercapacitor exhibits high hemocompatibility with hemolysis rate <5 %, good anticoagulant performance with coagulation time of 63.4 s, reasonable cycle stability with capacitance retention rate of 76.24 % after 20, 000 cycles, and supplies power for implanted heart rate sensors in female mice. This work provides a platform for implantable electronics to achieve anticoagulant activity in vivo.

To meet the demands of personalized medicine, implantable bioelectronics have garnered significant interest and attention^{1,2}. Among these, as a type of implantable energy storage device, implantable supercapacitors offer the advantages of high-power density and long cycle life. They can provide energy supply for bioelectronic devices within the body, which is crucial to the field of biomedicine^{3–5}. However, when an implanted device enters the human body, it inevitably comes into direct contact with blood, triggering the activation of multiple reaction mechanisms that impair the performance of the implanted energy storage device and potentially lead to serious adverse clinical events⁶. This includes thrombotic and thromboembolic complications caused by platelet activation, coagulation cascade,

and inflammation⁷. Therefore, the implanted supercapacitors must possess enough anticoagulant properties to prevent the occurrence of thrombosis or other cardiovascular and cerebrovascular diseases after implantation⁸.

Widely known, electrodes and electrolytes are important components of supercapacitors. The selection of active substances in electrode materials directly determines whether implantable supercapacitors can function normally in vivo and exhibit remarkable hemocompatibility⁹. Compared to other electrode materials like carbon-based materials, metal oxides, and hydroxide materials, conductive polymers are widely used in organic electronics, optoelectronic devices, sensors, and energy storage devices^{10,11} due to their

State Key Laboratory of Advanced Processing and Recycling of Non-ferrous Metals, School of Materials Science and Engineering, Department of Polymeric Materials Engineering, Lanzhou University of Technology, Lanzhou 730050 Gansu, China. ✉e-mail: ranfen@lut.edu.cn; ranfen@163.com

perfect electrical conductivity, light density, good flexibility, large specific surface area, and ease of processing¹². In particular, as an electrode material for supercapacitors, they show great biocompatibility¹³. Among these, poly(3, 4-ethylenedioxythiophene) (PEDOT) is polymerized from a certain amount of ethylenedioxythiophene (EDOT) monomer. This thienyl derivative is easy to prepare, low in cost, stable, and has high biocompatibility^{14–16}, attracting widespread attention in the fields of supercapacitor electrode materials^{17,18}.

Nevertheless, when used as an electrode material for implantable supercapacitors, PEDOT often requires doping to guarantee its conductivity¹⁹. During the chemical oxidation polymerization process of EDOT, it is oxidized to a conductive state with positive charge carriers. At this time, negatively charged counterions are doped in the molecules of EDOT⁺ to balance these positive charges or holes and improve its conductivity²⁰. These counterions are called dopants and include low molecular weight anions, polymer counterions, and biomacromolecules²¹, especially various polysaccharides have been studied as an important branch of biomacromolecules due to their exceptional biocompatibility^{22–26}. Among them, the biomacromolecule heparin (Hep) contains a large number of sulfonic acid groups with negatively charged, which could serve as counterions to balance the oxidized positive charge carriers of PEDOT and improve its electrical conductivity during the polymerization process²⁷. At the same time, compared to the poor stability and weak anticoagulant performance of small molecule dopants, the unique polysaccharide structure and abundant sulfonic acid groups of heparins effectively bind to anticoagulant enzymes, further reducing or inhibiting clotting enzyme activity and achieving an anticoagulant effect²⁸. As a result, the conductivity and hemocompatibility of an electrode material can be improved simultaneously by doping PEDOT with heparin as the counterion.

In this study, an anticoagulant supercapacitor has been designed into an all-in-one, where the anticoagulant macromolecule heparin is used as the counterion to dope PEDOT to prepare a bioelectrode material PEDOT: Hep with anticoagulant activity via chemical oxidation polymerization. The all-in-one anticoagulant supercapacitor is prepared through in situ polymerization, where the PEDOT: Hep and bacterial cellulose are used as the electrode and electrolyte layer. This supercapacitor exhibits good biological activity, anticoagulation performance, cycle stability, and electrochemical performance, and supplies the necessary electrical energy for implanted heart rate sensors due to introducing the anticoagulant macromolecule heparin. It

addresses the issues of poor electrochemical stability and the risk of coagulation or thrombosis in implantable energy storage devices. At the same time, the unique all-in-one structure provides a platform for implantable electronic devices to extend and operate stably in vivo.

Results

Anticoagulant mechanism of anticoagulant supercapacitor in vivo

With the rapid advancement of electronic technology, implantable electronic devices have become generally prevalent in the prevention, detection, diagnosis, and treatment of clinical diseases due to their high flexibility, safety, stability, and miniaturization²⁹. As such, implantable electronic devices must not only meet extraordinary electrical performance standards, but also satisfy biocompatibility requirements, especially hemocompatibility, to cope with the complex internal environment of the human body^{6,30}. Figure 1 illustrates that when traditional implantable bioelectronics enter the human body or direct contact with blood, the lack of antithrombotic protection mechanism on their surface can trigger a series of adverse clinical reactions, such as platelet activation, protein adsorption, inflammatory response, and thrombus formation⁷. These clinical reactions result in the accumulation of blood clots on the implant surfaces, impairing or reducing the electrical performance of electronic devices. Additionally, clots travel to the lungs or brain, causing embolism and systemic complications. Currently, anticoagulants or antiplatelet drugs are usually used to alleviate thrombosis when implanted materials or devices are used clinically, but the use of these drugs carries a risk of bleeding³¹.

To mitigate the risk of thrombosis and bleeding after implanting energy storage devices, heparin as a natural macromolecule is chosen to dope PEDOT and obtain the PEDOT: Hep as electrode material for implantable supercapacitor. The sulfonic acid anions present in heparin serve as counterions to balance the charge of EDOT⁺, thereby promoting enhanced electrical conductivity and electrochemical performance of the PEDOT-based electrode material. Simultaneously, some sulfonic acid groups within the heparin molecular structure, which remain uninvolved in the doping process, still possess strong negative charges. Through the collaborative effect of unique polysaccharide structure and these remaining sulfonic acid groups of heparins tightly bind to the lysine and arginine residues on the surface of anticoagulant enzymes. This binding mode facilitates alterations in the spatial configuration of anticoagulant enzymes. Consequently, this interaction enhances the mutual activity of anticoagulant and

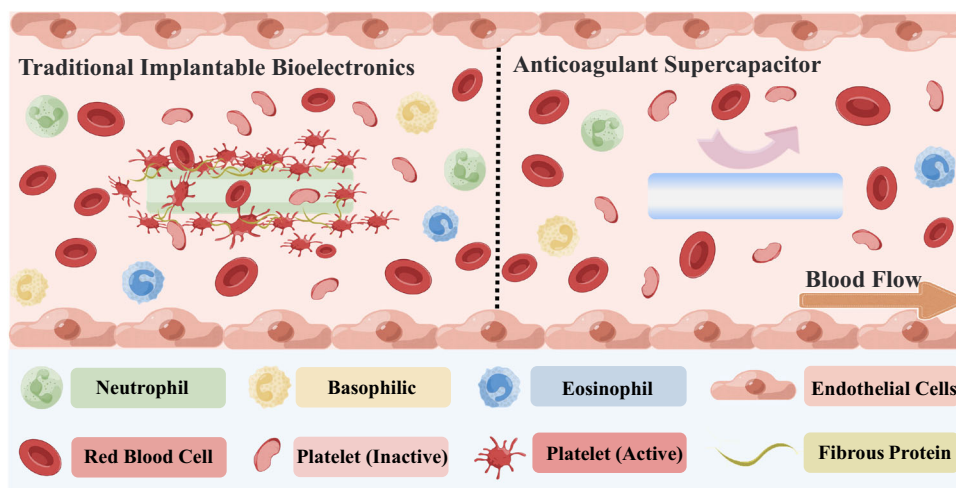


Fig. 1 | Different clinical responses of blood components when in contact with the traditional implantable bioelectronics and the anticoagulant implantable supercapacitors. The green device on the left is traditional implanted bioelectronics, the blue device on the right is anticoagulant supercapacitor, the orange

arrow shows the direction of blood flow, and the pink arrow indicates that the anticoagulant supercapacitor inhibits platelet adhesion. The cartoon module is by Figdraw (www.figdraw.com).

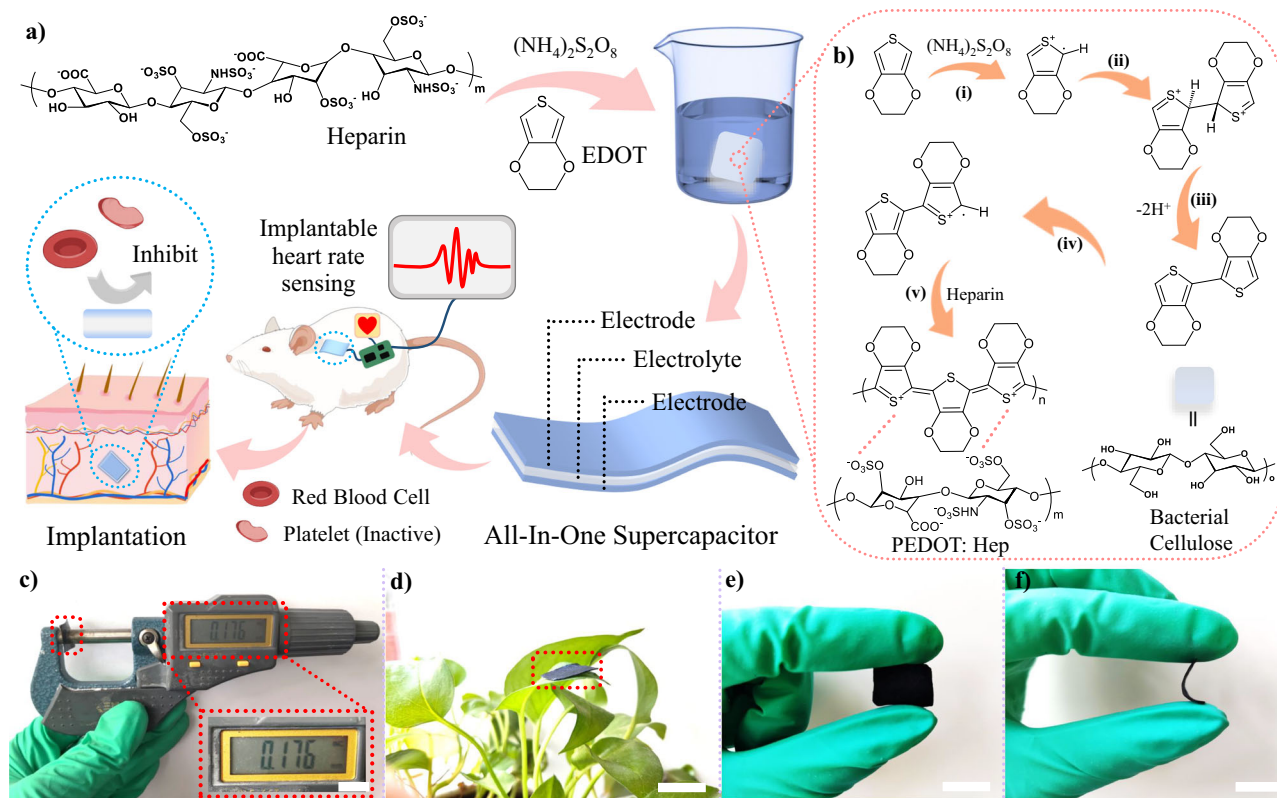


Fig. 2 | Preparation process and photographs of anticoagulant supercapacitor.

a Preparation and application schematic diagrams of bioelectrode material PEDOT: Hep and implantable anticoagulant supercapacitor (the pink arrow shows the preparation, implantation, and application of the anticoagulant supercapacitor, and the gray arrow indicates the anticoagulant supercapacitor inhibits platelet adhesion), **b** Schematic description of the oxidative polymerization of EDOT into PEDOT and heparin-doped PEDOT: (i) oxidation of EDOT to form cationic radicals,

(ii) dimerization of cationic radicals, (iii) deprotonation to form dimers, and (iv, v) oxidation of the PEDOT and heparin-doped PEDOT, respectively (the orange arrow shows the polymerization process of EDOT and the doping of heparin during the in situ polymerization of the supercapacitor), and **c–f** the thickness, placed on plant leaves photographs, front, and side photographs of anticoagulant supercapacitor, respectively, the scale bar is 1 cm. The cartoon mouse is by Figdraw (www.figdraw.com).

coagulation enzymes, resulting in a more than 2000-fold increase in the deactivation efficiency of coagulation enzymes^{7,8}. Currently, heparin is the preferred anticoagulant in clinical treatments for venous thromboembolism, acute coronary syndrome, and arterial thrombotic diseases such as coronary heart disease and cerebral thrombosis, effectively reducing the risk of thrombus formation. Based on this, the bioelectrode material is prepared by doping PEDOT with anticoagulant macromolecule heparin as counterion, designing the all-in-one implantable supercapacitor with high anticoagulant activity through in situ polymerization in this work. This supercapacitor not only meets the necessary electrochemical performance requirements of implantable supercapacitor, providing the necessary electrical energy for heart rate sensors after implantation, but also effectively prevents the activation of the blood coagulation pathway, and the occurrence of adverse clinical reactions such as platelet adhesion, thrombosis, and inflammation when implanted in the body or in direct contact with blood. This work provides a reference for the clinical application of implantable supercapacitors.

Synthesis mechanism, preparation, and characterization of PEDOT: Hep

The bioelectrode material of PEDOT: Hep is prepared via chemical oxidative polymerization of anticoagulant macromolecular heparin (Hep) and conductive polymer monomer ethylenedioxythiophene (EDOT) in the presence of ammonium persulfate (APS); and those with the different feed ratios and reaction time are shown in Supplementary Table S1. Subsequently, PEDOT: Hep and bacterial cellulose (BC) are used as the electrode and electrolyte layer, respectively, and the all-in-

one anticoagulant supercapacitor is obtained through in situ stepwise polymerization of EDOT on the surface of BC as flexible support substrate³². The anticoagulant supercapacitor provides the necessary electrical energy for the implanted heart rate sensor, and exhibits good anticoagulant performance, fulfilling the actual clinical needs (Fig. 2a).

Figure 2b and Supplementary Fig. S1 illustrates the oxidative polymerization of EDOT and the process of heparin-doped PEDOT. Generally, the conduction mechanism of intrinsically conductive polymers involves the delocalized migration of linear conjugated π electrons formed by alternating single and double bonds on the main chain, providing the possibility for electron movement within the polymer³³. However, the molecular orbital energy of the π bonds in PEDOT molecules is low, hindering the free movement of π electrons and affecting its conductivity¹⁹. To improve the conductivity of PEDOT, electrons must migrate from its valence band or be added to the conduction band to form soliton carriers, altering the distribution state of holes and free electrons in PEDOT. This process of electron migration is known as doping^{21,34,35}. Among them, oxidation dopants are introduced into PEDOT, and PEDOT acts as an electron acceptor to absorb electrons from its π -bond orbital, which is called *p*-type doping³⁶. The doping process involves charge transfer or an oxidation chemical reaction, resulting in the loss of electrons from the conjugated π bond, and doping increases the number of carriers in the PEDOT system to significantly enhancing its electrical conductivity³⁷. In this work, $(\text{NH}_4)_2\text{S}_2\text{O}_8$ is employed in the chemical polymerization of oxidation EDOT, and EDOT monomer is oxidized by $\text{S}_2\text{O}_8^{2-}$ ions into a cationic radical, which initiates the ladder growth polymerization of EDOT as shown in (i). In a classical stepwise polymerization, the

cationic radical undergoes dimerization, as shown in (ii), and is stabilized through the removal of two protons, as shown in (iii). The resulting PEDOT is ultimately doped with a large number of SO_3^- anion radicals contained in heparin as counterions to achieve the purpose of charge balance, forming heparin-doped PEDOT for PEDOT: Hep as shown in (iv) and (v)^{38,39}. During this process, the abundant sulfonic acid groups of heparins serve as counterions to balance the charge of EDOT^+ , improving the conductivity of PEDOT through chemical oxidative polymerization and doping^{27,40}. Moreover, the unique polysaccharide structure and sulfonic acid group contained in heparin effectively bind with antithrombin, enhancing the anticoagulant performance of PEDOT. When the anticoagulant supercapacitor made of PEDOT: Hep as a bioelectrode material is implanted in a mouse, its coagulant surface effectively inhibits the occurrence of platelet activation, coagulation cascade, and inflammatory response, reducing the risk of thrombosis and infection to deal with complex body fluid or blood environments.

Traditional gel-based supercapacitors formed by stacking layers under external force, these devices have macroscopic interfaces between multiple interfaces of electrode-electrolyte-electrode, which reduces the transport of charges and ions between the anion and the anode, resulting in poor electrochemical performance and interlayer slippage that severely impairs device performance. In this work, the anticoagulant supercapacitor with an all-in-one structure is obtained by directly constructing the electrode on both sides of the electrolyte layer through in situ polymerization, and improved the efficient transmission of ions or electrons to enhance the overall electrochemical performance. The distinctive all-in-one structure has high integrity to avoid the phenomenon of slipping caused by the steric effect between interfaces. At the same time, since the original BC membrane is pre-treated by a drying method at a high temperature (100 °C), the intermolecular hydrogen bonds are formed and connect individual fibers and strands through the evaporation of water in the BC membrane. Therefore, due to the irreversibility of evaporative drying, the water content and water retention capacity of the BC membrane cannot be restored by rehydration⁴¹. After being immersed in DI water for 7 days, the geometric size, thickness, and weight of both the original BC membrane and the all-in-one supercapacitor based on the BC membrane have nothing changed, indicating that the geometry of the BC membrane or the device have good structural stability (Supplementary Figs. S2, S3). The supercapacitor has an overall device thickness of only 0.176 mm, which is rare in the field of gel-based supercapacitors. Devices prepared by the same method exhibit similar thickness; these results also confirm the repeatability of the preparation method (Fig. 2c and Supplementary Fig. S4). In addition, the device is lightweight and can be easily placed on plant leaves (Fig. 2d), and has good mechanical flexibility and stability, maintaining a fully all-in-one state even when bent due to its special monolithic structure (Fig. 2e, f). This work provides prerequisites for the development of portable, wearable, and implantable electronics.

Anticoagulant macromolecular heparin acted as a counterion to dope PEDOT to balance its charge and guarantee its conductivity. As shown in Fig. 3a, due to the structure of heparin is rich in carboxyl ($-\text{COOH}$) and sulfonic acid ($-\text{SO}_3^-$), the FTIR of PEDOT: Hep exhibits characteristic absorption peaks of $\text{C}-\text{O}-\text{S}$, $\text{S}=\text{O}$, and $\text{C}-\text{O}-\text{C}$ bonds at 1329, 1184, and 1046 cm^{-1} , respectively. This provides preliminary confirmation that the bioelectrode material of PEDOT: Hep has been successfully prepared⁴². Heparin acts as the counterion of PEDOT and its sulfonic acid group is negatively charged to balance the oxidized EDOT^+ through electrostatic interaction. As a result, the decomposition temperature of PEDOT: Hep increases from 354 to 365 °C after introducing heparin to dope PEDOT, confirming the successful preparation of PEDOT: Hep (Fig. 3b). From the XPS analysis of PEDOT and PEDOT: Hep presented in Fig. 3c, it can be further observed that the peak intensities of S, O, and N elements in the spectrum of PEDOT: Hep are significantly stronger than that of PEDOT, indicating that heparin

rich in sulfonic acid groups has been successfully introduced into PEDOT. The peaks of $\text{S } 2p_{3/2}$ and $\text{S } 2p_{1/2}$ are noticed at 163.9 and 165.1 eV in the S element spectrum of PEDOT (Fig. 3d), and the S element high-resolution spectrum of PEDOT: Hep prepared by introducing heparin also exhibits distinct peaks of $-\text{SO}_x$ at 168.8 and 170.0 eV, confirming the presence of sulfonic acid groups and the introduction of heparin into the system. Similarly, due to the addition of heparin rich in sulfonic acid groups, the spectrum of O element high-resolution spectrum shows that the peak intensity at 531.7 eV is significantly enhanced compared to that of PEDOT (Fig. 3e), further confirming that a large number of $\text{S}=\text{O}$ bonds are provided by heparin in the PEDOT: Hep system. More importantly, compared with the unobvious peak intensity of the N element high-resolution spectrum of PEDOT, the spectrum of PEDOT: Hep has obvious peaks of $-\text{NH}_x$ at 400.5 and 401.8 eV due to bring in heparin⁴³. Therefore, the successful doping of PEDOT with heparin is also confirmed (Fig. 3f).

Scanning electron microscopy (SEM) clearly shows that due to heparin acting as the counterion to dope PEDOT during the chemical oxidation polymerization, the exposed sulfonic acid groups with negatively charged heparins can combine with the positive charge of the oxidized EDOT (EDOT^+) under electrostatic interaction. Compared to the dense morphology of PEDOT (Fig. 3g, h), the morphology of PEDOT: Hep becomes loose and porous with heparin attached to the surface of PEDOT in the form of microspheres (Fig. 3i, j). Based on the transmission electron microscopy (TEM) and dynamic light scattering (DLS, Malvern ZS90, UK) presented in Supplementary Figs. S5, S6 and Tables S2, S3^{27,44–48}, the PEDOT: Hep system exhibits a uniformly dispersed nanoscale particle morphology. Furthermore, the size of PEDOT: Hep (260.43 ± 0.74 nm) is comparable to that of commercial PEDOT: PSS (225 to 287.50 nm), indicating that the introduction of heparin enhances the dispersion of the PEDOT system. Additionally, compared to PEDOT (12.8 mV) with positive potential, the zeta potential of the PEDOT: Hep system is -21.3 mV (Supplementary Fig. S7 and Table S3), within or near the zeta potential range of commercial PEDOT: PSS (-19.0 to -55.6 mV). The increased absolute value of the zeta potential demonstrates that the dispersed PEDOT: Hep system is more stable and exhibits stronger resistance to aggregation²⁷. Furthermore, it can be clearly seen that the PEDOT system exhibits pronounced layering after static settling for 7 days, 30 days, and centrifugation at $102.78 \times g$ for 5 min, respectively (Supplementary Figs. S8, S9). This is due to the poor dispersion of the PEDOT system in water and its tendency to aggregate. In contrast, the PEDOT: Hep system maintains stable dispersion properties, with a distinct peak observed at 800 nm in the ultraviolet absorption spectrum using a UV-Vis spectrophotometer (UV-1600), the absorbance retention of PEDOT: Hep dispersed system ($>80.39\%$) is similar to the PEDOT: PSS dispersed system and extensively higher than that of PEDOT²⁷ (Supplementary Fig. S10). Consequently, the PEDOT: Hep dispersed system exhibits good dispersion and anti-aggregation characteristics during practical usage, providing a favorable foundation for enhancing the conductivity of PEDOT. In addition, compared to the water contact angle of PEDOT is 91.73° , the hydrophilicity of bioelectrode material PEDOT: Hep (the water contact angle is 48.75°) has significantly improved after doping with heparin, which is rich in functional groups (Supplementary Fig. S11). Based on this, N_2 adsorption and desorption experiments are carried out at 77 K by the BET method. According to the adsorption data, compared with PEDOT without heparin, the average adsorption pore size of PEDOT: Hep increased from 14.62 to 31.07 nm, respectively. As shown in Fig. 3k, PEDOT mainly exists in the form of mesopores and micropores, and the proportion of mesopores in PEDOT: Hep is greatly reduced, and micropores dominated after doping heparin (Fig. 3l). The N_2 adsorption-desorption curves for PEDOT and PEDOT: Hep exhibit a remarkable resemblance to Type II isotherms (Supplementary Fig. S12), which reflects the typical physical adsorption process observed on non-porous or macropores

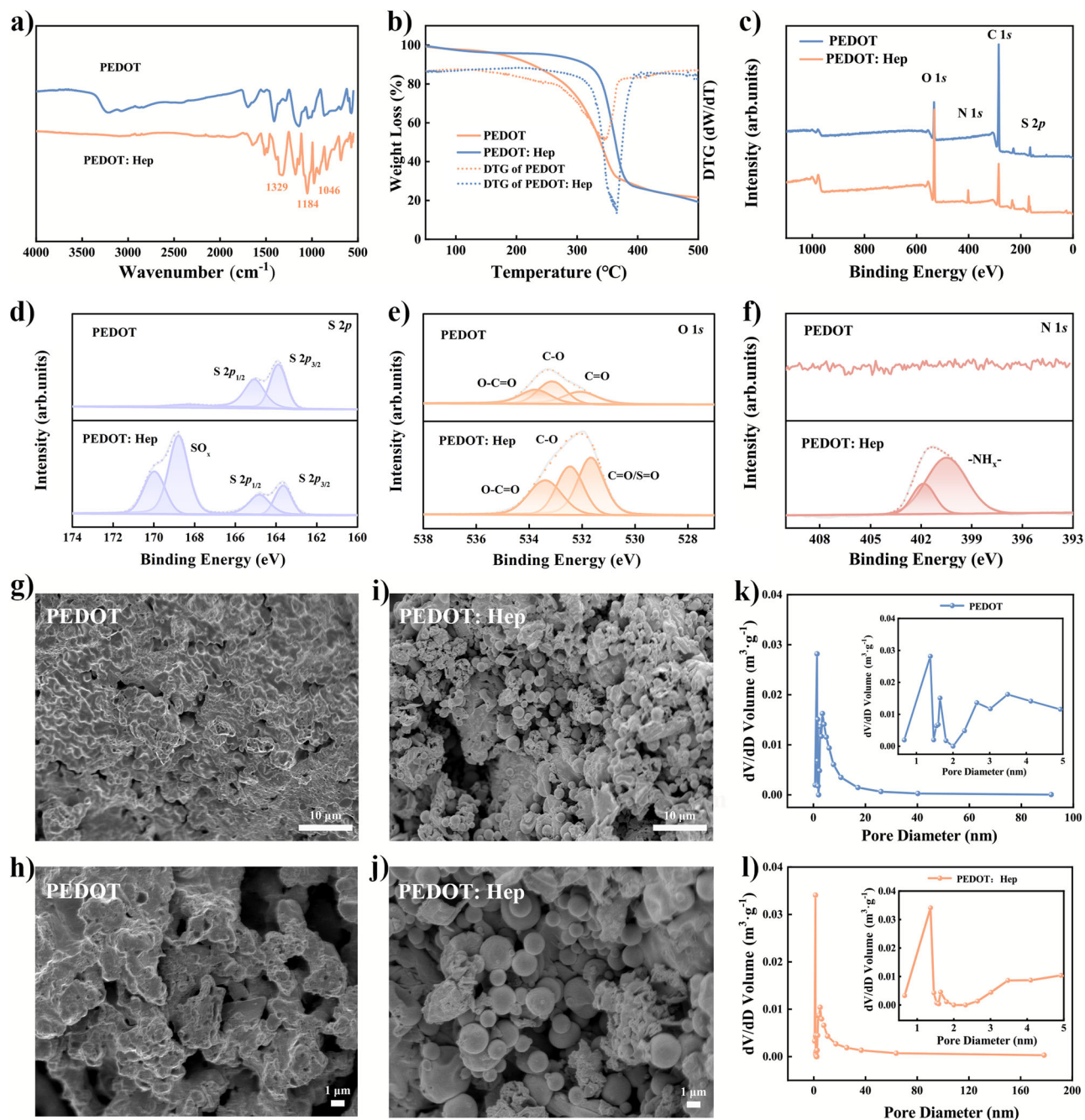


Fig. 3 | Characterization of PEDOT: Hep. **a** FTIR spectra, **b** TGA and DTG curves, **c** XPS spectra, **d** S 2p XPS spectra, **e** O 1s XPS spectra, **f** N 1s XPS spectra, **g**, **h** SEM of PEDOT, **i**, **j** SEM of PEDOT: Hep, **k** pore size distributions of PEDOT, and **l** pore size

distributions of PEDOT: Hep. The similar results are repeated in three independent experiments (**g–j**).

adsorbents^{49,50}. When micropores are present on the material surfaces, the specific surface area calculated using the BET method is inaccurate under these conditions. Based on this, although it can be clearly observed from the SEM image that the surface of PEDOT: Hep is looser and porous than that of PEDOT, the specific surface area of PEDOT: Hep ($22.03 \text{ m}^2\text{-g}^{-1}$) is slightly higher than that of PEDOT ($21.96 \text{ m}^2\text{-g}^{-1}$).

Conductivity, electrochemical properties, and hemocompatibility of PEDOT: Hep

The introduction of heparin increasing the porosity and specific surface area of PEDOT is confirmed by SEM and BET tests, providing a prerequisite for improving the electrochemical performance of PEDOT: Hep as an electrode material. The conductivity of PEDOT: Hep

prepared with varying heparin doping contents is evaluated using the four-probe (ST2263) method. PEDOT is a conductive polymer with an alternating conjugated structure of single and double bonds. Its natural state is often that of an insulator with a large bandgap, where electrons are confined to the conjugated π orbital or valence band, hindering transport and migration under an external electric field²⁷. As shown in Fig. 4a, the conductivity of PEDOT without heparin doping is weak at only 0.50 S m^{-1} . Upon oxidation, EDOT loses electrons to form positively charged EDOT^+ , and doped heparin with abundant sulfonic acid groups and negative charges to form multi-ion complexes through strong electrostatic association. This allows PEDOT to gain electrons and exhibit directional movement under an external electric field, endowing it with high conductivity²⁷. Consequently, the

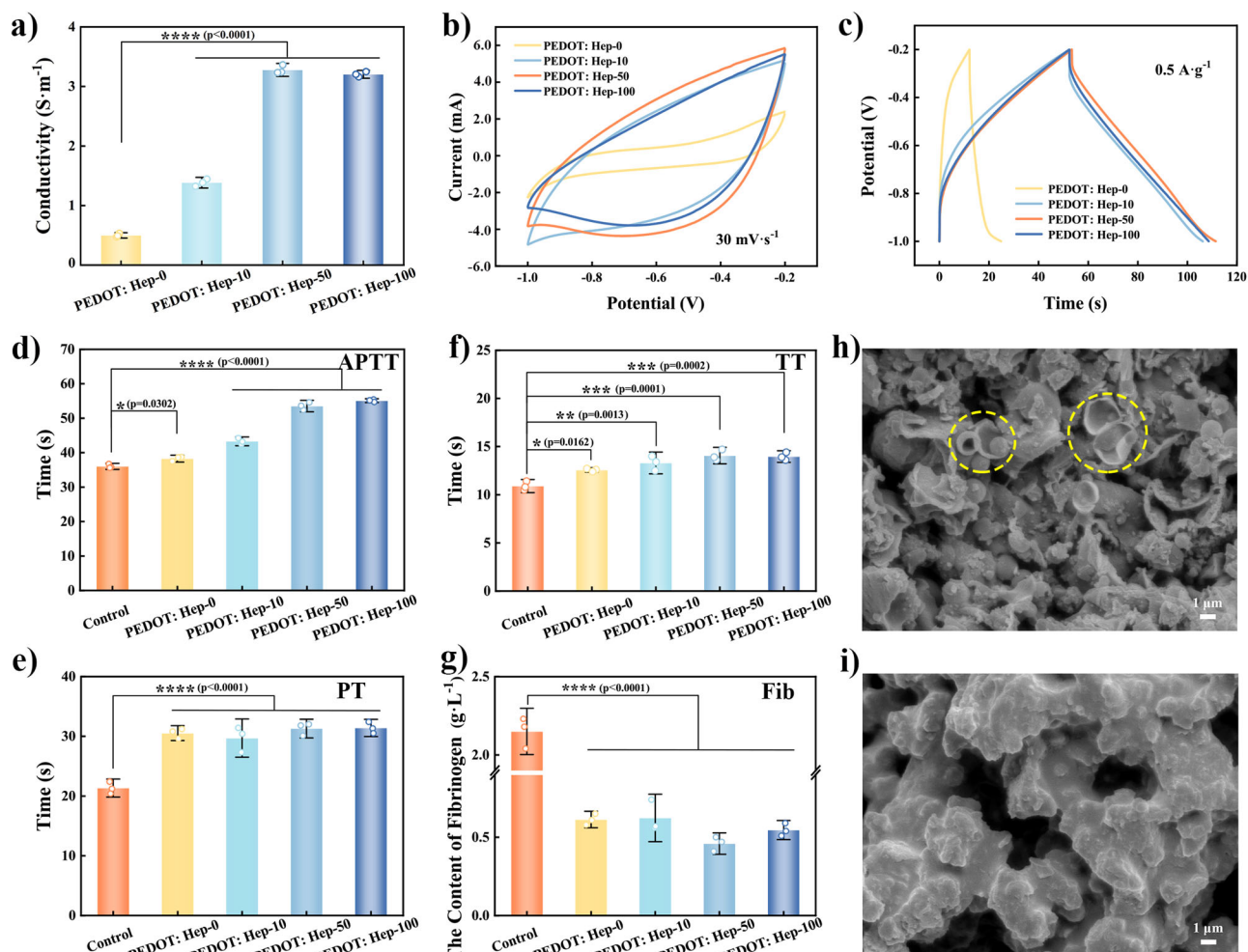


Fig. 4 | Electrochemical performance and hemocompatibility of PEDOT: Hep. **a** Conductivity, **b** CV curve at $30\text{ mV}\cdot\text{s}^{-1}$, **c** GCD at $0.5\text{ A}\cdot\text{g}^{-1}$; the anticoagulant performance of PEDOT: Hep: **d** activated partial thromboplastin time (APTT), **e** prothrombin time (PT), **f** thrombin time (TT), **g** fibrinogen content (Fib); and the platelet adhesion SEM of **h** PEDOT, and **i** PEDOT: Hep (the yellow circle shows the

attached platelets). Data were presented as mean \pm SD ($n = 3$ independent samples) (**a**, **d**–**g**). Statistical analysis by one-way ANOVA with Turkey's multiple comparisons test ($*p < 0.05$, $**p < 0.01$, $***p < 0.001$, and $****p < 0.0001$ indicate statistical significance) (**a**, **d**–**g**). The similar results are repeated in three independent experiments (**h**, **i**).

incorporation of heparin greatly enhances its electrical conductivity reaching a maximum of $3.27\text{ S}\cdot\text{m}^{-1}$. The possibility of introducing heparin to dope PEDOT to improve the conductivity of the electrode material PEDOT: Hep is further verified by cyclic voltammetry (CV) and galvanostatic charging-discharging (GCD). After introducing different doping amounts of heparin into PEDOT, a series of electrochemical performance tests are carried out as electrode materials by a three-electrode method. It can be seen from Fig. 4b that at a scan rate of $50\text{ mV}\cdot\text{s}^{-1}$, the area enclosed by the CV curve with increasing heparin content (0 to 100 mg) significantly increases. Similarly, when the specific current is $0.5\text{ A}\cdot\text{g}^{-1}$, the GCD curves of PEDOT: Hep with different heparin doping contents also exhibit a gradually increasing trend of reversible charging and discharging behavior (Fig. 4c). However, combining Fig. 4b, c and Supplementary Fig. S13, the electrochemical performance of PEDOT: Hep-100 decreases compared to PEDOT: Hep-50 electrode materials when the heparin content further increases from 50 to 100 mg. It can be seen from the analysis of XPS that PEDOT: Hep-50 and PEDOT: Hep-100 have highly consistent peak intensities in the full spectrum and S element high-resolution spectrum, especially the $-\text{SO}_x$ at 168.8 and 170.0 eV^{43} (Supplementary Fig. S14). This indicates that the doping sites of EDOT^+ approached saturation when the doping amount of heparin is 50 mg, and little contribution to the electrochemical improvement of the PEDOT: Hep

by continuing to add heparin content. Subsequently, PEDOT: Hep-50 is selected as the optimal condition and a series of electrochemical performance tests also confirmed its excellent electrochemical activity as an electrode material⁵¹ (Supplementary Fig. S15). Therefore, doping with heparin greatly improves the electrochemical performance of PEDOT as an electrode material.

On the other hand, heparin as an anticoagulant macromolecule is widely used in the field of clinical treatment of cardiovascular and cerebrovascular diseases and anticoagulant modification on implantable materials or device surfaces. In this work, the coagulation time of the bioelectrode material PEDOT: Hep is tested by APTT, PT, TT, and Fib to discuss whether it can meet the anticoagulant performance requirements in the implantation field as a bioelectrode material. From Fig. 4d–g, it can be seen that compared with the blank control group, the APTT, PT, and TT of the electrode materials obtained by doping with different amounts of heparin are all prolonged and the Fib is decreased, which confirms the introduction of heparin significantly improve the anticoagulation performance of the electrode material PEDOT: Hep. Specifically, heparin as an anticoagulant macromolecule has a unique polysaccharide structure and abundant sulfonic acid groups. These features enable it to effectively bind with the characteristic motif of antithrombin and primarily act on the intrinsic coagulation pathway to enhance anticoagulant activity⁵². Meanwhile, it

can be clearly seen from Fig. 4h that the surface of the PEDOT electrode material without heparin lacks a protective mechanism against platelet adhesion, and the platelet adhesion phenomenon is clearly visible in the SEM images; but the introduction of heparin effectively abolished platelet adhesion (Fig. 4i). Thus, from the hemocompatibility of PEDOT: Hep as electrode materials, it is evident that the introduction of heparin endows bioelectrode materials with good hemocompatibility, especially anticoagulation and antiplatelet adhesion properties.

The bioelectrode material PEDOT: Hep prepared in this study incorporates heparin as a counterion doping PEDOT to balance charge and enhance its electrochemical performance. And leveraging potent sulfonic acid groups of heparins, PEDOT: Hep binds to characteristic motifs of anticoagulant enzymes, further reducing or inhibiting thrombin activity and achieving anticoagulant properties. Consequently, compared to other PEDOT: negatively charged polysaccharide systems, PEDOT: Hep exhibits advantages in terms of dispersion, anti-aggregation, conductivity, and biocompatibility, particularly anticoagulant performance^{23,27} (Supplementary Table S4). Considering this study focuses on simultaneously enhancing and balancing conductivity, electrochemical properties, and anticoagulant activity, the PEDOT: Hep-50 as the optimal condition is chosen to conduct subsequent research.

Structural characteristics, biocompatibility, and hemocompatibility of anticoagulant supercapacitors

Subsequently, PEDOT: Hep-50 and bacterial cellulose (BC) are utilized as the components of electrode and electrolyte layer, respectively, and the anticoagulant supercapacitor with all-in-one structure of supercapacitor is prepared via in situ polymerization. Specifically, the schematic diagram, optical microscope, and SEM images of the supercapacitor structure are shown in Supplementary Fig. S16a–c. Since the original BC membrane is pre-treated by drying (100 °C), its internal structure, such as the dense cellulose nanofiber network observed in the BC cross-sectional SEM image in Supplementary Fig. S16c, prevents the EDOT monomer from excessive penetration or immersion during the controlled polymerization time, and the EDOT monomer is only deposited and polymerized on or near the surface of the BC layer⁵³. Therefore, the interior of the BC membrane remains in a non-conductive state and can be used as an electrolyte layer to construct an all-in-one supercapacitor, and observed in optical microscope and SEM images that EDOT monomer only polymerizes and grows on both sides of the BC layer. In contrast, the traditional sandwich-type supercapacitor obtained by stacking electrode-electrolyte-electrode layers, the all-in-one supercapacitor constructed by directly introducing electrodes on both sides of the electrolyte layer via in situ polymerization macroscopically blurs the interface of electrode-electrolyte-electrode. The steric hindrance effect at the electrode-electrolyte interface of the supercapacitor with an all-in-one structure is significantly reduced and the transport of electrolyte ions between the interfaces is obviously improved⁵⁴, positively impacting electrochemical reaction progress. At the same time, the special all-in-one structure prevents potential misalignment and detachment between components during continuous strain deformation, avoiding serious consequences of equipment failure. The stress-strain curve in Supplementary Fig. S17 confirms the impressive mechanical properties of the supercapacitor, with a stress of 13.20 MPa at a strain of 35.47%, meeting the mechanical performance requirements of implantable flexible devices⁵⁵. This generation of energy storage devices is expected to be applied in the implantable field and attract more and more attention.

The morphologies of the constructed supercapacitor are microscopically observed using SEM. Obviously, the fiber morphology of BC as an electrolyte layer before polymerization is shown in Supplementary Fig. S18a. The supercapacitor is integrated by constructing electrode materials on both sides of the electrolyte layer via in situ

polymerization, resulting in a transformation of surface morphology from fibrous to rough granular, which is characteristic of electrode materials (Supplementary Fig. S18b). The SEM cross-section of the supercapacitor presented in Fig. 5a reveals a closely interconnected electrode-electrolyte-electrode structure forming a whole. Corresponding element mapping of C and O elements are uniformly distributed across the entire cross-section of the supercapacitor, while the S element is only distributed at both ends of the electrode side. This is due to the electrolyte layer being composed of bacterial cellulose, containing only C, H, and O elements, while the electrode material of PEDOT: Hep encompasses a substantial quantity of S elements in addition to C, H, and O elements. As such, the distribution of the S element is confined to the electrode layers on both sides, further corroborating the successful fabrication of the supercapacitor with an all-in-one structure. The supercapacitor obtained via in situ polymerization in this study effectively eliminates the macroscopic interface between the electrode and electrolyte layer, enhancing the electrochemical performance and overall stability of the device.

The supercapacitor obtained via in situ polymerization in this study effectively eliminates the macroscopic interface between electrode-electrolyte-electrode, enhancing the electrochemical performance and overall stability of the device. However, to better control the depth of polymerization and prevent device short-circuiting, the polymerization time is optimized to 12, 24, 36, and 48 h, respectively, to obtain supercapacitor-12, supercapacitor-24, supercapacitor-36, and supercapacitor-48. By optimizing the interfacial polymerization preparation strategy, the interface issue of supercapacitors is resolved and greatly benefiting the practical application of implantable energy storage devices.

Traditional dopants of PEDOT primarily consist of PSS or small molecules, which are acidic (The pH of PEDOT: PSS is 4.42) or prone to decomposition after doping, and causing adverse effects on cells and tissues²⁷. When heparin replaces the acidic PSS, the pH of the PEDOT: Hep dispersion system approaches neutrality (pH = 6.80), which greatly enhances the biological safety of the system (Supplementary Fig. S19). By selecting natural macromolecule heparin as a dopant for PEDOT, effectively addresses these issues and endows the electrode materials and devices with good biocompatibility and hemocompatibility. Figure 5b, c intuitively presents the growth and vitality of L929 cells incubated in the extract of the anticoagulant supercapacitor. The cells exhibit a normal spindle morphology at both 24 and 48 h. Moreover, there is a noticeable increase in cell count with the extension of incubation time, and the relative proliferation rate of the cells is greater than 83%. This confirms that the PEDOT: Hep-based anticoagulant supercapacitors have excellent biocompatibility. Furthermore, the hemolysis rate of all the anticoagulant supercapacitors prepared with different polymerization time are much lower than the ASTM standard (ASTM F756-2008) requirement for the hemolysis rate of biomaterials (<5%)⁵⁶, meeting clinical implanted devices hemocompatibility requirements (Fig. 5d). Figure 5e also shows that compared to the control group, the APTT, PT, and TT of supercapacitors obtained with different polymerization time are significantly prolonged, and the Fib content gradually decreased or remains similar to the control group. This indicates that with prolonged polymerization time, heparin content in bioelectrode material of PEDOT: Hep deposited on the supercapacitor surface is gradually increases, effectively inhibiting coagulation processes and improving anticoagulant activity. Surprisingly, the APTT of supercapacitor-36 is 63.4 s when the polymerization time is 36 h, and the extension of APTT confirms that heparin mainly acts on the intrinsic coagulation pathway⁸. This is mainly due to the fact that heparin contains a large number of negatively charged sulfonic acid groups, which combine with the characteristic motifs of antithrombin to act on the anticoagulation process. As shown in Supplementary Fig. S20, the original BC membrane has a very low clotting time (APTT is only 29.3 s). Although the PSS molecule also contains abundant sulfonic acid groups and is used as a heparin-

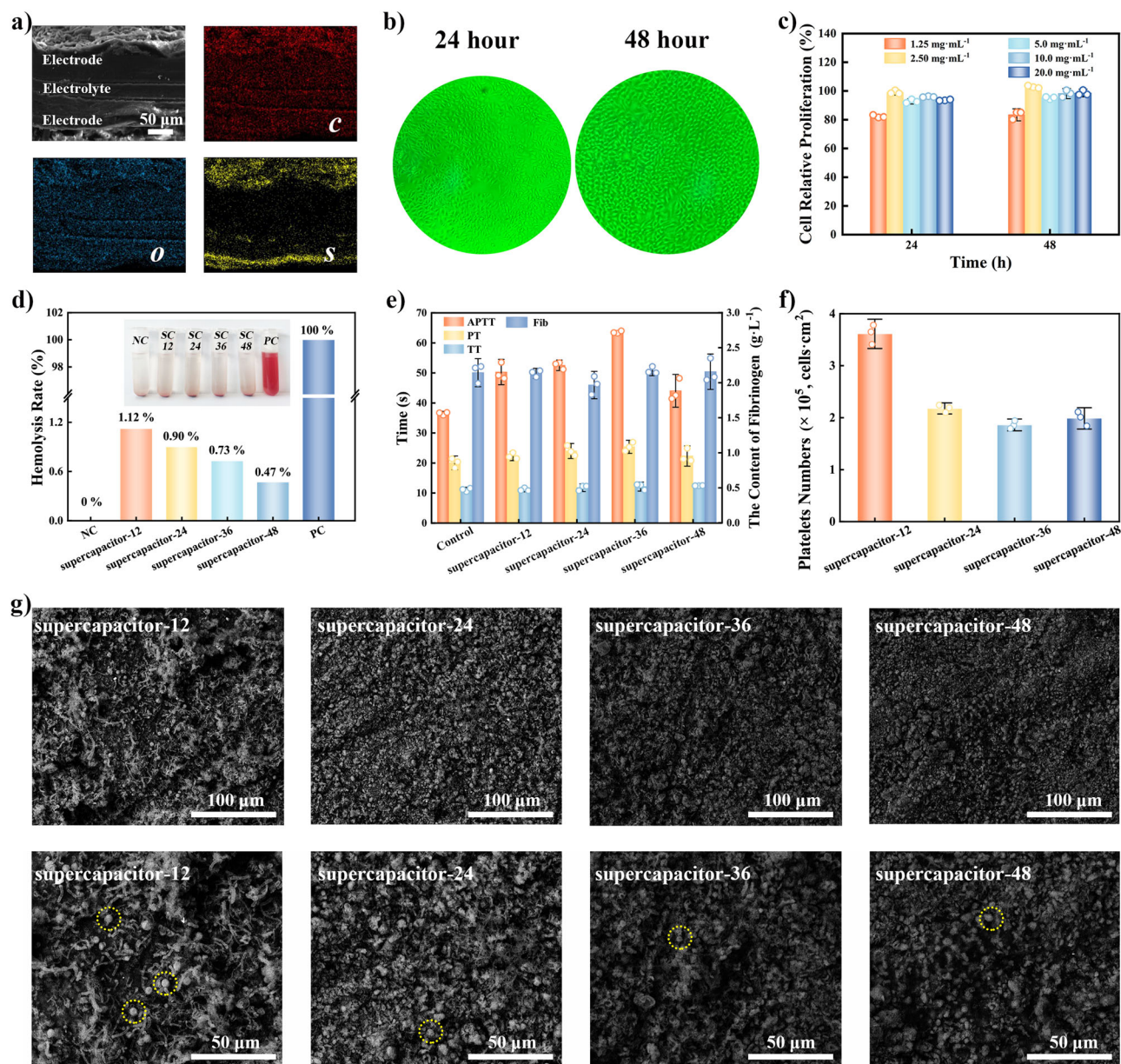


Fig. 5 | Structural and hemocompatibility of anticoagulant supercapacitors. **a** Cross-section SEM of anticoagulant supercapacitor with all-in-one structure and element mapping of C, O, and S element, respectively; the biocompatibility and hemocompatibility of anticoagulant supercapacitor; **b** digital photographs of the growth of L929 cells at 24 and 48 h, respectively; **c** cell proliferation at different concentrations measured by cck-8 method; **d** the hemolysis rate (HR) (PC refers to

a positive control (DI water), and NC refers to negative control (normal saline)), **e** anticoagulant performance, **f** platelets numbers, and **g** the SEM of platelet adhesion (the yellow circle shows the attached platelets). The similar results are repeated in three independent experiments (**a**, **b**, **g**). Data were presented as mean \pm SD ($n = 3$ independent samples) (**c**, **e**, **f**).

mimicking polymer to improve the anticoagulant effect⁵⁷, the coagulation time of the PEDOT: PSS/BC (APTT is 46.4 s) based on PEDOT: PSS as electrode material is lower than that of PEDOT: Hep/BC (APTT is 63.4 s). This is mainly due to the unique polysaccharide structure of heparin and its abundant sulfonic acid, which greatly improves its binding ability to the characteristic motifs of antithrombin, thus endowing PEDOT: Hep-based electrode materials and supercapacitors with strong anticoagulant effect. Meanwhile, Fig. 5f, g respectively display the platelet adhesion test and the platelet adhesion number of supercapacitors with anticoagulant performance obtained at different polymerization time. Among then, the number of platelets adhering to the surface of the supercapacitor significantly decreases with the extension of the polymerization time. This is mainly due to the gradual increase in the content of the bioelectrode material PEDOT: Hep

deposited on the electrolyte layer interface with the extension of polymerization time in a certain time range. However, further prolonging the polymerization time beyond this time limit will lead to excessive penetration of electrode material into the electrolyte layer, leading to reduced deposition of heparin-containing PEDOT: Hep on both sides of the BC membrane and deteriorating its anticoagulation performance. Therefore, strictly controlling the polymerization time is critical for maintaining good anticoagulant properties in the device.

The electrode material PEDOT: Hep contains a large amount of heparin, which has a special polysaccharide structure and abundant sulfonic acid groups that bind with the anticoagulant thrombin base sequence, effectively enhancing anticoagulant activity and reducing platelet adhesion⁵⁸. The reduction of platelet adhesion and the prolongation of coagulation time confirms that the device can achieve

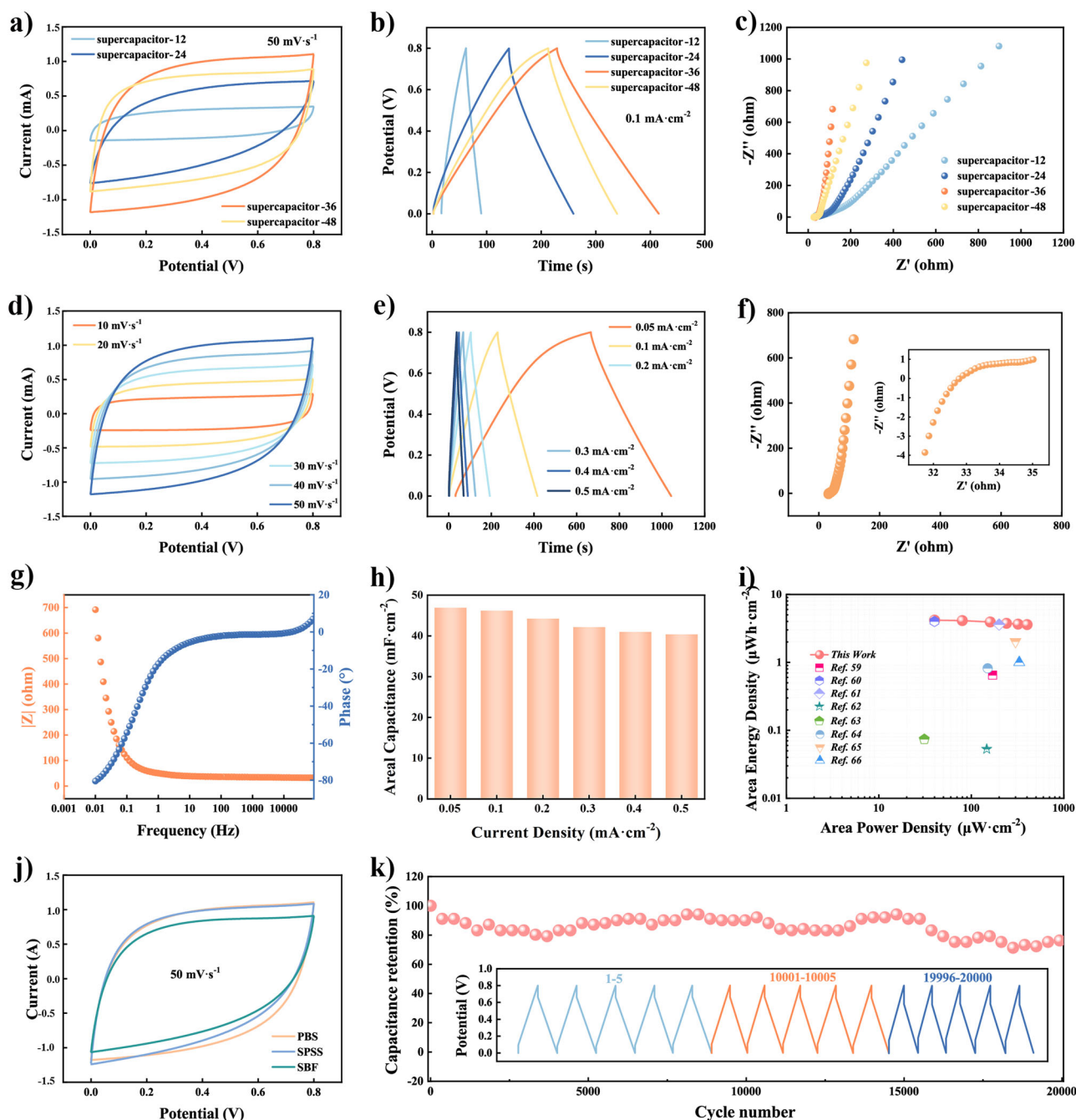


Fig. 6 | Electrochemical performance of anticoagulant supercapacitor. **a** CV curve at 50 mV s^{-1} , **b** GCD at 0.1 A g^{-1} , **c** Nyquist plots, **d** CV curves at different scan rates, **e** GCD curves at different specific currents, **f** Nyquist plots, **g** Bode plots, **h** areal capacitance at different specific currents, **i** Ragone plots of areal energy

density and power density, **j** CV curve in a different electrolyte solution (phosphate-buffered saline (PBS), stroke-physiological saline solution (SPSS), and simulated body fluid (SBF)) at 50 mV s^{-1} , and **k** cyclic stability.

excellent anticoagulant performance due to importing anticoagulant macromolecular heparin acting on the intrinsic coagulation pathway. Therefore, as the attention to the hemocompatibility of implantable energy storage devices, especially the anticoagulant performance, the supercapacitor with anticoagulant activity designed in this work provides a prerequisite and solid foundation for normal operation of implantable energy storage devices in vivo.

Electrochemical properties of anticoagulant supercapacitors

The in situ polymerization time and depth not only affect the hemocompatibility of supercapacitors, but also have a certain impact on their electrochemical performance. As shown in Fig. 6a, as

polymerization time increases from 12 to 36 h, the CV curves of the supercapacitor-12 to supercapacitor-36 gradually become quasi-rectangular and symmetrical at a scan rate of 50 mV s^{-1} . The GCD curve also gradually presents a relatively symmetrical triangle at a specific current of 0.1 A g^{-1} , and the area surrounded by the triangle increases with the prolongation of the polymerization time, indicating that the supercapacitor has good coulombic efficiency and reversible charging and discharging behavior (Fig. 6b). Nyquist plots in Fig. 6c clearly show that the Warburg impedance in the low-frequency region due to electrode diffusion decreases significantly with increased polymerization time. This is mainly because the interfacial effect between the electrode and electrolyte layer is reduced with prolonged

polymerization time, and a fast ion transport channel can be formed between the interface, which provides favorable conditions for improving the electrochemical performance of the supercapacitor. Unfortunately, the CV curves, GCD curves, and Nyquist plots reveal the electrochemical performance of the supercapacitor-48 is significantly reduced when the polymerization time is extended from 36 to 48 h. This is mainly due to the sulfur (S) element only contained in the PEDOT: Hep is excessively permeated and diffused into the electrolyte layer with the extension of polymerization time, and the interface between the electrode and the electrolyte layer becomes blurred (Supplementary Fig. S21). The distribution and content of S elements on the surface (Supplementary Figs. S22, S23), and the peak intensity of -SO_x at 168.6 and 169.8 eV of supercapacitor-48 is significantly lower than that of supercapacitor-36⁴³ (Supplementary Fig. S24). This indicates that long polymerization time leads to excessive penetration of PEDOT: Hep into the BC electrolyte layer, which easily causes the precursor of short circuits and adversely affects the device's performance. Therefore, the polymerization time must be strictly controlled to avoid this negative phenomenon. Under the same preparation conditions, electrochemical tests are conducted on three groups of supercapacitor-36. As shown in Supplementary Fig. S25 and Table S5, the three groups of supercapacitors are highly similar to the supercapacitor-36 shown in Fig. 6a–c in terms of electrochemical performance and yield. This indicates that by introducing electrode materials directly on both sides of the electrolyte layer through in situ polymerization to build a supercapacitor with an all-in-one structure, this manufacturing method has high repeatability and reproducibility, and the preparation method is simple, which can be used for mass production. Therefore, the hemocompatibility and electrochemical performance of supercapacitors obtained at different polymerization times are considered, the in situ polymerization time is controlled at 36 h to obtain the supercapacitor-36, which has best electrochemical performance and hemocompatibility.

Figure 6d confirms that the CV curves of supercapacitor-36 are symmetric within the voltage range of 0 to 0.8 V and scan ranges of 10–50 mV·s⁻¹, exhibiting minimal distortion across different scan rates and indicating ideal capacitive performance. Within the range of 0.05 to 0.5 mA·cm⁻², the GCD curves reveal ideal reversible charging-discharging behavior. As current density increases, none of the GCD curves exhibit voltage drop, confirming the strong electrochemical stability of supercapacitor-36 (Fig. 6e). Furthermore, the maximum operating voltage of this supercapacitor can be extended to 1.2 V (Supplementary Fig. S26). To accommodate various application scenarios, it quickly completes the charging process within 25 to 30 s at 0.1 mA·cm⁻², and achieves discharging behaviors lasting for 168, 201, and 622 seconds at specific currents of 0.1, 0.05, and 0.01 mA·cm⁻², respectively, resulting in mismatched charging and discharging curves. In practical applications, rapid charging of supercapacitors and slow discharging of the required power supply devices are achieved, greatly satisfying diverse application needs (Supplementary Fig. S27). The Nyquist and Bode diagrams in Fig. 6f, g show that the charge transfer resistance (semicircular in the high-frequency area) and diffusion resistance (straight line in low-frequency area) of the device are low. This reflects the interfacial compatibility between the electrolyte layer and electrode material, indicating that supercapacitor-36 exhibits good performance in the field of energy storage.

According to the GCD curve and formula (6), Fig. 6h indicates that the areal specific capacitances are 46.96, 46.24, 44.28, 42.18, 41.02, and 40.42 mF·cm⁻² at 0.05 to 0.5 mA·cm⁻², respectively, with a capacitance retention rate of 86.07%. Figure 6i and Supplementary Table S6 display the supercapacitor areal energy densities are 39.98 and 400.25 μWh·cm⁻² when the areal power densities are 4.17 and 3.59 μW·cm⁻², respectively, which are higher than most reported PEDOT-based supercapacitors^{59–66}. Subsequently, similar and stable electrochemical performance of anticoagulant supercapacitors in different electrolyte solutions (PBS, SPSS,

SBF, and whole blood) are presented in Fig. 6j and Supplementary Figs. S28, 29. The capacitance retention of the device remained at 76.24% after 20, 000 GCD cycles (Fig. 6k). The supercapacitor has a stable interfacial cross-linked structure compared to other conventional flexible supercapacitors, effectively reducing ion transport barrier to avoid charge loss between the electrode and electrolyte during the charging and discharging processes⁶⁷. The GCD curves for different cycle numbers show high consistency, further confirming the exceptional cycle stability of the anticoagulant supercapacitor during charging and discharging. At the same time, the CV and GCD curves of the supercapacitor do not significantly change at different bending angles (180°, 155°, 135°, and 115°), which is an excellent performance for flexible devices (Supplementary Fig. S30). To further increase the output voltage and capacitance, one feasible method is to connect multiple supercapacitors in series or parallel. For example, the voltage can rise to 2.5 V or even more when two identical supercapacitors are connected in series, meeting the specific energy or power requirements (Supplementary Fig. S31). In conclusion, the electrochemical properties displayed by this supercapacitor provide a solid foundation for stable and long-term operation of energy storage devices in vivo.

Applications of anticoagulant supercapacitor

Implantable biomedical monitoring systems can detect and regulate physiological and pathological parameters, such as heart rate, respiratory rate, and blood pressure, achieving early diagnosis and prevention of diseases⁶⁸. Currently, implantable batteries or supercapacitors remain the main power source for most implantable electronic devices⁶⁹. While these implantable power devices meet electrical performance, few studies focus on their hemocompatibility, especially anticoagulation performance. This leads to the thrombus formation on the surface of the implanted power device due to its lack of anticoagulant protection, which easily causes pulmonary embolism or cardiovascular embolism after implantation. Interestingly, the anticoagulant supercapacitor designed in this work effectively solves this issue. On the one hand, the supercapacitor provides the necessary electrical energy for the normal operation of implantable bioelectronics. On the other hand, it exhibits excellent anticoagulation performance, avoiding the formation of thrombus after implantation. The schematic diagram and digital photograph of the anticoagulant supercapacitor connected to the heart rate sensor are shown in Fig. 7a, b. Subsequently, the anticoagulant supercapacitor implanted in the subcutaneous tissue of the mouse can effectively provide energy for the implantable heart rate sensor and realize real-time detection and transmission of heart rate signals (Fig. 7c, d, Supplementary Movie 1, and Supplementary Fig. S32). To further evaluate the effectiveness of this anticoagulant supercapacitor, the device is implanted in the subcutaneous area of the mouse to power the electronic device (Fig. 7e). After charging, it can successfully light up the LED light (threshold voltage is 1.2 V) (Fig. 7f and Supplementary Movie 2). This demonstrates its ability to provide power for bioelectronics in the future. At the same time, electrochemical performance tests before and after 24 h also found that the areal capacitance of the supercapacitor has only degraded by 25.3% (Fig. 7g–i). The decrease in capacitance may be related to the infiltration of mouse body fluids, but the decrease can be improved by appropriate packaging strategies²⁹.

Self-discharging as an inherent property of supercapacitors is a thermodynamic spontaneous process driven by the ion concentration and electric field gradient near the electrode surface^{70,71}. The self-discharging rate of supercapacitors constructed from PEDOT-based electrode materials obtained under different dopants has been evaluated. Among them, the supercapacitors of PEDOT: Hep/BC and PEDOT: PSS/BC are charged in a potential window of 0 to 0.8 V under an applied current of 0.1 mA, and their open circuit potential (OCP) changes within 5 h are recorded. As shown in Supplementary Fig. S33a, the OCP decay of the PEDOT: Hep/BC is significantly slower than that

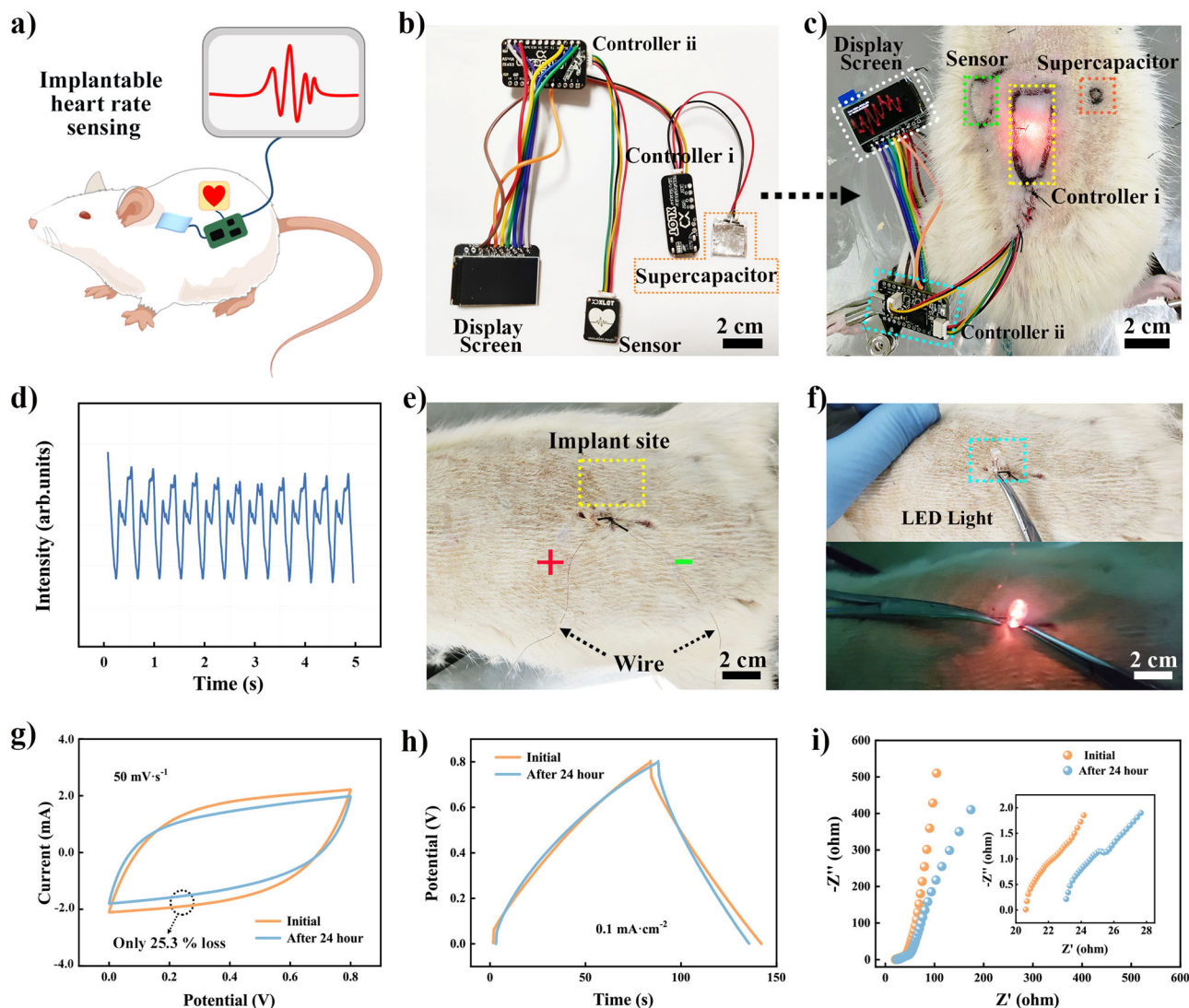


Fig. 7 | Applications of anticoagulant supercapacitor. **a, b** Schematic diagram and digital photograph of supercapacitor connected to heart rate sensor, **c** digital photograph of the implanted heart rate sensor powered by supercapacitor implanted subcutaneously in the mouse, **d** record heart rate monitoring signals from the

implantable heart rate sensor powered by a supercapacitor, **e** digital photograph of the supercapacitor implanted subcutaneously in the mouse, **f** LED light is powered by supercapacitor, and **g–i** the CV, GCD, and Nyquist curves before and after 24 h of implantation supercapacitor. The cartoon mouse is by Figdraw (www.figdraw.com) (**a**).

of the PEDOT: PSS/BC. After 5 h, the PEDOT: Hep/BC and PEDOT: PSS/BC drop from 0.8 to 0.28 and 0.17 V, respectively, and the OCP decay rate of the PEDOT: Hep/BC is 17.72% lower than that of the PEDOT: PSS/BC. This result indicates that the self-discharging rate of the supercapacitor based on PEDOT: Hep is lower. At the same time, the leakage current of the supercapacitor at 0.8 V is measured, and is shown in Supplementary Fig. S33b, the leakage currents of the PEDOT: Hep/BC and PEDOT: PSS/BC gradually stabilize at 0.83 and 0.71 μ A after 2 h, respectively, and the leakage current of the PEDOT: Hep/BC is smaller than that of the PEDOT: PSS/BC, further proving that the self-discharging rate of the supercapacitor doped with the biomacromolecule heparin is lower compared to other PEDOT-based supercapacitors. In addition, in actual clinical applications, it is possible to suppress the self-discharging phenomenon and obtain anticoagulant supercapacitors more suitable for implantable bioelectronics by optimizing the electrolyte or separator based on this⁷².

Long-term stability of anticoagulant supercapacitors in vivo

Supercapacitors are implanted into mice to evaluate their long-term stability, biocompatibility, and hemocompatibility in vivo, especially their anticoagulation properties. The schematic diagram and digital

photographs of the supercapacitor implanted into the mouse are shown in Fig. 8a, b, respectively. Subsequent observations revealed that the mice can carry out normal daily activities on the 15th and 90th day after the supercapacitors are implanted, with normal hair growth and no inflammation at the implantation site. When the device is removed on the 15th and 90th day after implantation, there is no obvious tissue adhesion to the surface of the supercapacitor at the implantation site (Fig. 8b and Supplementary Figs. S34, S35). Meanwhile, the device maintains similar surface integrity and cross-sectional layered morphology before and after 90 days of immersion in simulated body fluid (SBF) (Supplementary Figs. S36, S37). These results confirm that the supercapacitors exhibit good structural stability, integrity, biocompatibility, and hemocompatibility. Hematology analyses are performed on the mouse in the blank control group and on the 15th and 90th day after supercapacitor implantation, respectively. The blood clotting analyses are shown in Fig. 8c that the coagulation time and fibrinogen content on the 15th and 90th day post-implantation are similar to or slightly increased compared to the blank group. This indicates that the anticoagulant supercapacitor does not cause cardiovascular diseases such as blood clotting and thrombus after implantation. At the same time, blood routine tests are found in

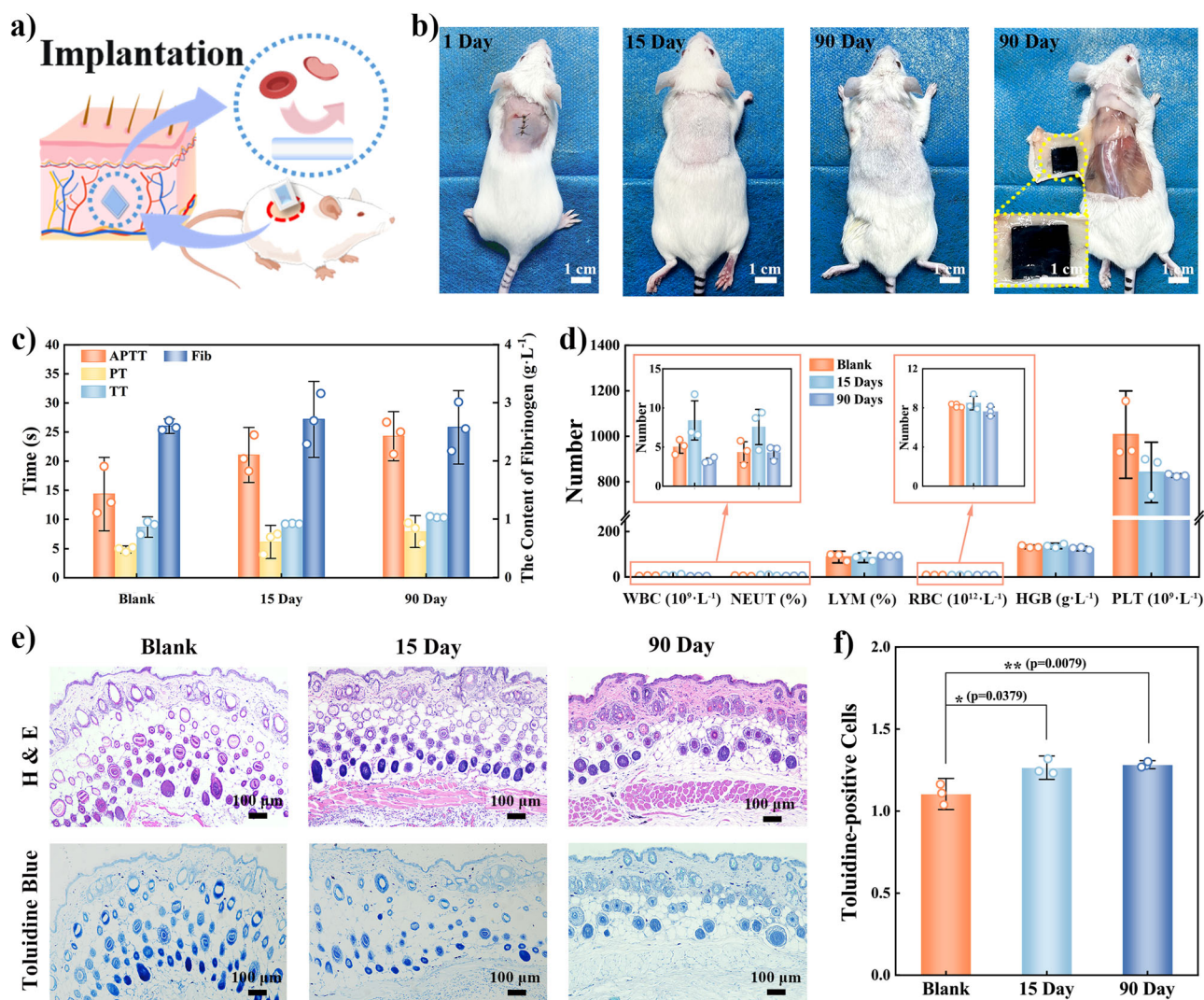


Fig. 8 | Hemocompatibility and biocompatibility of anticoagulant supercapacitors in vivo. **a** Schematic diagram of implantation, **b** digital photograph of the 1st day, 15th day, 90th day after implantation, and the dissection on 90th day after implantation, **c** anticoagulant performance, **d** blood routine (WBC white blood cell count, NEUT neutrophils, LYM lymphocytes, RBC red blood cell count, HGB hemoglobin concentration, and PLT platelet count), **e** H&E and toluidine blue

staining at the implant regions on the blank control and implanted tissues, and **f** statistical analysis of mast cells of the blank control and implanted tissues. The cartoon mouse is by Figdraw (www.figdraw.com) (**a**). The similar results are repeated in three independent experiments (**b**, **e**). Data were presented as mean \pm SD ($n = 3$ independent samples) (**c**, **d**, **f**). Statistical analysis by one-way ANOVA with Turkey's multiple comparisons test (* $p < 0.05$ and ** $p < 0.01$) (**f**).

Fig. 8d and Supplementary Table S7. The number of red blood cells, white blood cells, and platelet count in the blank group and implanted with supercapacitor are similar, further confirming that no inflammation and thrombosis are induced after long-term implantation⁷³.

Afterwards, histological analyses are conducted on the implantation sites. H&E and toluidine blue staining, as shown in Fig. 8e and Supplementary Fig. S38, there is no inflammatory response in the tissue at the implantation sites at 15th and 90th day post-implantation compared to the blank control group. The mast cells are observed by toluidine blue staining to represent the degree of inflammation, and the statistical analysis of mast cells is shown in Fig. 8f that there is no significant difference between the blank control group and the implantation group. Through the anticoagulant performance, blood routine, and pathological analysis of mice 90 days after implantation, it can be confirmed that the supercapacitors still maintain good biocompatibility and hemocompatibility, especially anticoagulant activity after 90 days of long-term implantation. Therefore, the heparin-doped PEDOT for anticoagulant supercapacitor evidences long-term stable biocompatibility and hemocompatibility after implantation, providing infinite possibilities for widespread application of implantable energy storage devices³.

Discussion

In summary, we have demonstrated an anticoagulant supercapacitor by heparin-doped PEDOT for potential applications in implantable bioelectronics. Heparin contains a large number of negatively charged sulfonic acid groups, which serve as counterions for PEDOT to balance its oxidized positive charge carriers and guarantee its conductivity. Additionally, heparin has a unique polysaccharide structure and abundant sulfonic acid group can effectively bind with the characteristic motif of antithrombin, reducing or blocking the activity of thrombin to achieve the purpose of anticoagulation. This study effectively combines the electrochemical properties of implantable energy storage devices with hemocompatibility, particularly anticoagulant activity. This addresses the issue of implantable energy storage devices lacking a thrombus protection mechanism in the body, which can result in blood coagulation, thrombus, and other threats to human health and affect the normal operation of the device. It provides a solution for the long-term stable operation of implantable energy storage devices in vivo. To transform the anticoagulant supercapacitor into a real biomedical application in the future, several challenges need to be addressed: the ability to integrate a wireless

charging system with the anticoagulant supercapacitors to solve the problem of charging in vivo; designing a highly acid-resistant supercapacitor to meet the complex application scenarios in vivo; supercapacitors used in the skull or cardiovascular system need to meet miniaturization requirements; implantable supercapacitors need to match the corresponding flexibility and mechanical stretchability according to the mechanical properties of the body tissues to achieve efficient and safe applications. By deeply designing the chemical functionalization of materials and energy devices, these challenges can be overcome, making the biocompatible power system fulfill the actual power supply requirements of bioelectronics.

Methods

Ethical statement

All animal procedures were performed in accordance with the National Research Council's Guide for the Care and Use of Laboratory Animals and were approved by the Animal Experimentation Ethics Committee of Laboratory Animal Ethics Committee of Zhejiang Haikang Biological Products Co., Ltd., and the approval ID was HKSYDWLL2021027.

Chemicals and materials

3, 4-ethylenedioxythiophene (EDOT, $M = 142.18$), heparin sodium (Hep, ≥ 150 USP units/mg, the content of sulfuric acid group is about 26%), bacterial cellulose (BC, the fiber diameter is 40 to 60 nm and the length is $> 20 \mu\text{m}$), ammonium persulfate (APS, $M = 228.201$) were obtained from Macklin Reagent, Beijing Labgic Technology Co., Ltd., Hainan Yide Co., Ltd., and Guangdong Guanghua Sci-Tech Co., Ltd., respectively. Phosphate-buffered saline (PBS, 1x), stroke-physiological saline solution (SPSS), and simulated body fluid (SBF) were purchased from Shanghai Yuanye Bio-Technology Co., Ltd. Commercial poly(3, 4-ethylenedioxythiophene): poly(styrene sulfonate) (PEDOT: PSS, P824250, 1.5% in water, Macklin Reagent) was used as a control material. All of the above chemicals were used as received unless otherwise specified.

Preparation of bioelectrode material of PEDOT: Hep

About 1.2 g EDOT and 50 mg Hep were dissolved in 100 mL DI water, and stirred at room temperature (25°C) for 2 h under a nitrogen (N_2) atmosphere. Then, 5 mL DI water containing 0.3 g APS as oxidant solution and added to the mixed solution, and stirring was continued at room temperature (25°C) for 48 h under N_2 atmosphere to obtain a dark blue solution to complete the polymerization. Then the solution was centrifuged under extreme centrifugal conditions ($10,278 \times g$ for 5 min) and washed three times with DI water and the mixture of acetone and methanol ($V_1: V_2 = 1: 7$), respectively, to remove unreacted EDOT monomers and further purify the electrode material³⁸. Finally, the black polymer was dried in a vacuum oven at 60°C for 24 h to obtain a bioelectrode material of PEDOT: Hep. The compositions of PEDOT: Hep were shown in Supplementary Table S1.

Preparation of anticoagulant supercapacitor of PEDOT: Hep/BC

About 1.2 g EDOT, 50 mg Hep, and BC ($10 \times 10 \times 0.135 \text{ mm}^3$) were immersed in 100 mL DI water, and stirred at room temperature (25°C) for 2 h under N_2 atmosphere. Then, 5 mL DI water containing 0.3 g APS as oxidant solution was dissolved and added to the mixed solution, and stirring was continued at room temperature (25°C) for 36 h under N_2 atmosphere to obtain a dark blue supercapacitor to complete the in situ polymerization⁷⁴. The compositions and polymerization time of the supercapacitors were listed in Supplementary Table S1.

Characterizations

The above fabricated bioelectrode material of PEDOT: Hep and anticoagulant supercapacitor were characterized by using various spectroscopic techniques. The molecular structure, morphology, X-ray photoelectron spectra (XPS), water contact angle, N_2 adsorption/desorption isotherms and pore distributions, element mapping, and

thermogravimetric performance of PEDOT: Hep and supercapacitor were characterized by FTIR (NEXUS670), scanning electron microscope (SEM JSM-6701 F), transmission electron microscope (TEM JEM-2010F), LSM 800 Laser Confocal Microscope, WCA PHS-3C, Brunauer-Emmett-Teller method (BET JW-BK200C), PerkinElmer PHI ESCA system, and thermogravimetric analysis (TGA NETZSCH, $10^\circ\text{C}\cdot\text{min}^{-1}$ in nitrogen atmosphere), respectively.

Mechanical property

The mechanical properties of the supercapacitor ($25 \times 15 \times 0.38 \text{ mm}^3$) were tested at room temperature (25°C) with a mechanical testing machine (TY8000B-500N, Jiangsu Tianyuan Test Equipment Co., Ltd.) at a rate of $10 \text{ mm}\cdot\text{min}^{-1}$. The tensile (σ , MPa) and strain (ε , %) of the supercapacitor were calculated by formula (1) and formula (2)¹⁸, respectively.

$$\sigma(\text{MPa}) = \frac{F}{A} \quad (1)$$

$$\varepsilon(\%) = \frac{L - L_0}{L_0} \times 100 \quad (2)$$

Where F , A , L_0 , and L were the force, cross-sectional area, initial length, and fracture length in tension of the supercapacitor, respectively.

Electrical conductivity

The electrical conductivity of PEDOT: Hep powder was tested using the four-probe method. Under a pressure of 60 MPa, 150 mg of PEDOT: Hep powder was compressed into a thin sheet. After 10 min of compression, the samples were placed on a fixture, ensuring their flatness. Subsequently, the four probes were individually in contact with the four corners of the sample at a temperature of 26°C and 42% humidity, and the electrical conductivity was recorded. This evaluation aimed to assess the electrical performance of the PEDOT: Hep as electrode material⁷⁵.

Electrochemical tests of PEDOT: Hep

The electrode material was prepared by mixing the PEDOT: Hep (80 wt %), acetylene black (8%), graphite (8%), and poly (tetrafluoroethylene) (4%)^{76,77}. Subsequently, the electrode material was coated on nickel foam ($1.0 \times 1.0 \text{ cm}^2$), each electrode contained 4 mg of PEDOT: Hep, and dried thoroughly (60°C , 12 h). The electrochemical tests of PEDOT: Hep were accomplished in the three-electrode system using an electrochemical workstation (CHI 660E), with the aforementioned prepared electrode material as a working electrode. Operating voltage between -1.0 to -0.2 V , cyclic voltammetry (CV) curves were tested across various scan rates (10 to $50 \text{ mV}\cdot\text{s}^{-1}$); galvanostatic charging-discharging (GCD) curves were evaluated at different specific currents (0.1 to $1.0 \text{ A}\cdot\text{g}^{-1}$). Additionally, electrochemical impedance spectroscopy (EIS) spectra were tested in a range of 10^{-2} – 10^5 Hz . The specific capacitance of PEDOT: Hep was evaluated from the GCD curve and formula (3); combined with their specific capacitance, formula (4), and formula (5), the corresponding mass-energy density and mass power density were achieved.

$$C_m = \frac{I \times \Delta t}{m \times \Delta V} \quad (3)$$

$$Em = \frac{C_m \times \Delta V^2}{7.2} \quad (4)$$

$$Pm = \frac{Em \times 3600}{\Delta t} \quad (5)$$

Where C_m , E_m , P_m , and m were specific capacitance ($\text{F}\cdot\text{g}^{-1}$), mass-energy density ($\text{Wh}\cdot\text{kg}^{-1}$), mass power density ($\text{W}\cdot\text{kg}^{-1}$), and mass (g) of the

PEDOT: Hep, respectively; I , Δt , and ΔV were discharging current (A), discharging time (s), and voltage (V), respectively.

Electrochemical tests of anticoagulant supercapacitor

The assembly and testing process of the anticoagulant supercapacitor were as follows¹⁸: two identical layers of carbon cloth ($1.0 \times 5.0 \text{ cm}^2$) as the current collector were placed on both sides of the supercapacitor (the volume is $1.0 \times 1.0 \times 0.135 \text{ cm}^3$, and the mass loading is 40 mg cm^{-2}) under pressure. Within the voltage range of 0 to 0.8 V, electrochemical tests of CV and GCD curves were conducted using CHI 660E in a two-electrode system under various scan rates (10 to 50 mV s^{-1}) and specific currents (0.05 to 0.5 mA cm^{-2}), respectively, and EIS spectra were tested in frequency range of 10^{-2} – 10^5 Hz . Cyclic stability tests were obtained through the LAND (CT2001A) instrument with 0.5 mA cm^{-2} . PBS, SPSS, and SBF solutions and whole blood of mouse were selected as the electrolytes for the supercapacitor, respectively. The areal capacitance of anticoagulant supercapacitor was calculated from their GCD curves and formula (6), and the corresponding areal energy density and areal power density were calculated from their areal capacitance, formula (7), and formula (8).

$$C_S = \frac{I \times \Delta t}{S \times \Delta V} \quad (6)$$

$$E_S = \frac{C_S \times \Delta V^2}{7.2} \quad (7)$$

$$P_S = \frac{E_S \times 3600}{\Delta t} \quad (8)$$

Where C_S , E_S , P_S , and S were areal capacitance (mF cm^{-2}), areal energy density ($\mu\text{Wh cm}^{-2}$), areal power density ($\mu\text{W cm}^{-2}$), and test area (cm^2) of an anticoagulant supercapacitor, respectively.

Cell culture

The cell viability was measured by the CCK-8 method to evaluate the survival and toxicity of anticoagulant supercapacitor on the mouse embryonic fibroblasts cell line (L929, Item No.: GNM2812, Servicebio Technology Co., Ltd). Firstly, $10 \mu\text{L}$ of sterile supercapacitor extracts of different concentrations were added to each well of the 96-well plates containing DMEM complete culture solution containing L929 cells (7500 cells/well , $1 \times 10^6 \text{ cells/mL}$), and then the 96-well plate at 37°C in a $5\% \text{ CO}_2$ incubator for 24 and 48 h. The absorbance (OD) of the 96-well plate at 450 nm was measured with an enzyme marker after incubation, and the relative proliferation of cells was calculated according to formula (9).

$$\text{Cell Relative Proliferation}(\%) = \frac{(OD_S - OD_C)}{(OD_N - OD_C)} \times 100 \quad (9)$$

Where OD_S , OD_C , and OD_N were the OD values of the samples, blank control, and negative control, respectively.

Hemolytic activity test

A hemolysis test was performed on the supercapacitor to evaluate its hemocompatibility¹⁸. Briefly, fresh mouse whole blood was diluted ($V_{\text{blood}}: V_{\text{saline}} = 1: 1.25$), and 0.3 mL of diluted whole blood was added to 2.7 mL of saline solution ($0.9\% \text{ NaCl}$) soaked in supercapacitor samples, DI water, and saline solution as the samples, positive control, and negative control, respectively. After incubated in a water bath at 37°C for 1 h, each group was centrifuged at $102.78 \times g$ for 5 min, and the optical density of the supernatant was measured at 545 nm using a UV-Vis spectrophotometer (UV-1600). The hemolysis rate (HR) was

calculated by formula (10).

$$HR(\%) = \frac{(OD_S - OD_N)}{(OD_P - OD_N)} \times 100 \quad (10)$$

Where OD_S , OD_N , and OD_P referred to the mean absorbance values of the supercapacitor, negative control, and positive control, respectively.

Anticoagulant test

Fresh blood from mice was collected with an anticoagulant vacuum tube ($V_{\text{sodium citrate}}: V_{\text{blood}} = 1: 9$), and the collected fresh blood was centrifuged at $925.02 \text{ g min}^{-1}$ for 15 min to obtain platelet-poor plasma (PPP).

The activated partial thromboplastin time (APTT), prothrombin time (PT), thromboplastin time (TT), and fibrinogen content (Fib) of PEDOT: Hep and supercapacitor were evaluated using an automatic coagulation analyzer (RAC-1830), respectively⁷⁸. Briefly, 10 mg of PEDOT: Hep and $1.0 \times 1.0 \text{ cm}^2$ of supercapacitor were placed in 3 mL of PBS solution ($\text{pH} = 7.4$) and incubated in a 37°C water bath for 24 h, respectively. Then the PBS solution was removed, 1 mL PPP was added, and incubation continued at 37°C for 30 min before transferring the PPP to the sample tube for use. APTT, TT, PT, and FIB were measured using an automatic coagulometer to evaluate the coagulation of PEDOT: Hep and supercapacitor.

Platelet adhesion test

Fresh blood from mice was collected and centrifuged at $411.12 \text{ g min}^{-1}$ for 5 min to obtain platelet-rich plasma (PRP). PEDOT: Hep and supercapacitor were immersed in PBS solution at 37°C for 24 h, then PEDOT: Hep and supercapacitor were removed and placed in $500 \mu\text{L}$ of PRP and incubated at 37°C for 2 h. The PRP was removed and PEDOT: Hep and supercapacitor were rinsed three times with PBS solution before being fixed with $4 \text{ wt}\%$ glutaraldehyde in PBS for 24 h at 4°C . After washed with PBS solution, the PEDOT: Hep and supercapacitor were dried and dehydrated through a series of gradient physiological alcohol/PBS solutions ($25, 50, 75, 85, 95$, and $100 \text{ V/V}\%$), the adhesion of platelets on the surface was observed by scanning electron microscopy (SEM JSM-6701 F)⁵⁸.

In vivo implantation experiment

Nine ICR mice (female) were purchased from the SPF Biotechnology Co., Ltd. (Beijing, China). Six-week-old pathogen-free mice ($20 \pm 5 \text{ g}$) were used throughout the in vivo studies (the Laboratory Animal Use Permit No. was SYXK Zhe 2021-0005, and the sex of animals was not associated with the results in this study). All mice were kept in a 12 h light/dark cycle animal room (the room temperature was 25°C , and the humidity was 55%) with free access to water and food for 7 days of adaptive feeding. After the adaptive feeding period, the mice were randomly divided into a blank group and an experimental group. The experimental mice were injected subcutaneously with pentobarbital sodium (7 mg mL^{-1}) to anesthetize the mice, and the anesthetic dose was based on the weight of the mice (0.01 mL g^{-1}). The response of the mice was observed to ensure that they were anesthetized. After anesthesia, skin preparation, depilation, and disinfection were performed on the dorsal side of the mice. An epidermis and dermis wound about 1 cm in length was created on the back of each mouse, and the anticoagulant supercapacitor was implanted subcutaneously and sutured. The mice were observed and fed according to their group after modeling, with the blank control group being fed normally without implantation. Digital photographs were taken of the wound sites of mice in the experimental group on the 1st, 15th, and 90th day after implantation, respectively.

In vivo blood routine and anticoagulation test

On the 15th and 90th day after implantation, blood routine tests were performed on mice in the experimental and blank control groups using a complete blood cell counter, including red blood cell count (RBC), hemoglobin concentration (HGB), mean corpuscular volume (MCV), mean corpuscular hemoglobin concentration (MCHC), mean platelet volume (MPV), hematocrit (HCT), mean corpuscular hemoglobin (MCH), platelet count (PLT), white blood cell count (WBC), and differential white blood cell count: neutrophils (NEUT), lymphocytes (LYM), monocytes (MON), eosinophils (EOS), and basophils (BASO)⁷³. The coagulation parameters (APTT, PT, TT, and Fib) were tested through the automatic coagulation analyzer.

Histopathological examination

The mice were sacrificed and the wound skin tissues at the implantation sites were collected on the 15th and 90th day after implantation and blank group. The tissues were sectioned according to standard tissue analysis methods and stained with H&E and toluidine blue for histopathological analysis to evaluate the biological safety of supercapacitors after implantation^{3,79}.

Data analysis

All experiments were performed at least three times ($n \geq 3$) independently, and the results were expressed as mean \pm standard deviation (SD). All statistical analyses were presented using Origin 2021 and Image-Pro Plus software. Multiple comparisons were performed using one-way analysis of variance (ANOVA). For all tests, $*p < 0.05$, $**p < 0.01$, $***p < 0.001$, and $****p < 0.0001$ indicate statistical significance, ns: no significance.

Reporting summary

Further information on research design is available in the Nature Portfolio Reporting Summary linked to this article.

Data availability

All relevant data were available within the article and Supplementary information. The data that support the findings of this study are available on request from the corresponding authors. Source data are provided with this paper.

References

- Yu, M. et al. Emerging design strategies toward developing next-generation implantable batteries and supercapacitors. *Adv. Funct. Mater.* **33**, 2301877 (2023).
- Strakosas, X. et al. Metabolite-induced in vivo fabrication of substrate-free organic bioelectronics. *Science* **379**, 795–802 (2023).
- Jang, Y. et al. Implantable biosupercapacitor inspired by the cellular redox system. *Angew. Chem., Int. Ed.* **60**, 10563–10567 (2021).
- Sheng, H. et al. A thin, deformable, high-performance supercapacitor implant that can be biodegraded and bioabsorbed within an animal body. *Sci. Adv.* **7**, eabe3097 (2021).
- Lee, Y. et al. Nano-biosupercapacitors enable autarkic sensor operation in blood. *Nat. Commun.* **12**, 4967 (2021).
- Chen, K. et al. Safety and effectiveness evaluation of flexible electronic materials for next generation wearable and implantable medical devices. *Nano Today* **35**, 100939 (2020).
- Liu, X. et al. Blood compatible materials: state of the art. *J. Mater. Chem. B* **2**, 5718–5738 (2014).
- Wang, X. et al. Anticoagulant macromolecules. *Macromolecules* **56**, 4387–4430 (2023).
- Azam, M. A. et al. Recent advances in biomass-derived carbon, mesoporous materials, and transition metal nitrides as new electrode materials for supercapacitor: A short review. *Int. J. Energy Res.* **45**, 8335–8346 (2021).
- Zhang, S. et al. Hydrogel-enabled transfer-printing of conducting polymer films for soft organic bioelectronics. *Adv. Funct. Mater.* **30**, 1906016 (2019).
- Bessaïre, B. et al. Synthesis of continuous conductive PEDOT: PSS nanofibers by electrospinning: a conformal coating for optoelectronics. *ACS Appl. Mater. Interfaces* **9**, 950–957 (2016).
- Nezakati, T. et al. Conductive polymers: opportunities and challenges in biomedical applications. *Chem. Rev.* **118**, 6766–6843 (2018).
- Ul Hoque, M. I. et al. Intrinsically conducting polymer composites as active masses in supercapacitors. *Polymers* **15**, 730 (2023).
- Jiang, Y. et al. Topological supramolecular network enabled high-conductivity, stretchable organic bioelectronics. *Science* **375**, 1411–1417 (2022).
- Volkov, A. V. et al. Understanding the capacitance of PEDOT: PSS. *Adv. Funct. Mater.* **27**, 1700329 (2017).
- Kayser, L. V. et al. Stretchable conductive polymers and composites based on pedot and PEDOT: PSS. *Adv. Mater.* **31**, 1806133 (2019).
- Gan, D. et al. Bioadhesive and electroactive hydrogels for flexible bioelectronics and supercapacitors enabled by a redox-active core-shell PEDOT@PZIF-71 system. *Mater. Horiz.* **10**, 2169–2180 (2023).
- Wang, X. et al. Integrating supercapacitor with sodium hyaluronate based hydrogel as a novel All-In-One wound dressing: self-powered electronic stimulation. *Chem. Eng. J.* **452**, 139491 (2023).
- Harris, A. R. et al. Effective area and charge density of chondroitin sulphate doped PEDOT modified electrodes. *Electrochim. Acta* **197**, 99–106 (2016).
- Leprince, M. et al. Design of hyaluronan-based dopant for conductive and resorbable PEDOT ink. *Carbohydr. Polym.* **301**, 120345 (2023).
- Donahue, M. J. et al. Tailoring PEDOT properties for applications in bioelectronics. *Mater. Sci. Eng. R Rep.* **140**, 100546 (2020).
- del Agua, I. et al. Conducting polymer iongels based on PEDOT and guar gum. *ACS Macro Lett.* **6**, 473–478 (2017).
- Mantione, D. et al. Poly(3, 4-ethylenedioxythiophene): glycosaminoglycan aqueous dispersions: toward electrically conductive bioactive materials for neural interfaces. *Macromol. Biosci.* **16**, 1227–1238 (2016).
- del Agua, I. et al. Conducting polymer scaffolds based on poly(3, 4-ethylenedioxythiophene) and xanthan gum for live-cell monitoring. *ACS Omega* **3**, 7424–7431 (2018).
- Ajjan, F. N. et al. High performance PEDOT/lignin biopolymer composites for electrochemical supercapacitors. *J. Mater. Chem. A* **4**, 1838–1847 (2016).
- Casado, N. et al. Electrochemical behavior of PEDOT/lignin in ionic liquid electrolytes: suitable cathode/electrolyte system for sodium batteries. *ChemSusChem* **10**, 1783–1791 (2017).
- Yu, C. et al. Ultra-histocompatible and electrophysiological-adapted PEDOT-based hydrogels designed for cardiac repair. *Adv. Funct. Mater.* **33**, 2211023 (2023).
- Lawanprasert, A. et al. Heparin-peptide nanogranules for thrombosis-actuated anticoagulation. *Small* **18**, 2203751 (2022).
- Sheng, H. et al. A soft implantable energy supply system that integrates wireless charging and biodegradable Zn-ion hybrid supercapacitors. *Sci. Adv.* **9**, eadh8083 (2023).
- Chen, X. et al. Stretchable supercapacitors as emergent energy storage units for health monitoring bioelectronics. *Adv. Energy Mater.* **10**, 1902769 (2019).
- Liu, J. et al. Anticoagulant activities of indobufen, an antiplatelet drug. *Molecules* **23**, 1452 (2018).
- Lv, X. et al. A new method to prepare no-binder, integral electrodes-separator, asymmetric all-solid-state flexible supercapacitor derived from bacterial cellulose. *J. Phys. Chem. Solids* **110**, 202–210 (2017).

33. Sakunpongpitiporn, P. et al. Tuning of PEDOT: PSS synthesis via multiple doping for enhanced electrical conductivity. *Polym. Int.* **70**, 1534–1543 (2021).
34. Eun, J. et al. Electrochemical doping and dedoping behaviors of PEDOT-based ternary conducting polymer composites with binary polymer surfactants. *ACS Appl. Polym. Mater.* **5**, 5495–5502 (2023).
35. Skorupa, M. et al. Dopant-dependent electrical and biological functionality of pedot in bioelectronics. *Polymers* **13**, 1948 (2021).
36. Chung, J. et al. 100th Anniversary of macromolecular science viewpoint: recent advances and opportunities for mixed ion and charge conducting polymers. *ACS Macro Lett.* **9**, 646–655 (2020).
37. Sheng, L. et al. Boosting PEDOT energy storage with redox dopant and electrolyte additive. *Chem. Eng. J.* **401**, 126123 (2020).
38. Khan, S. et al. Bio-hybrid blended transparent and conductive films PEDOT: PSS: chitosan exhibiting electro-active and antibacterial properties. *Eur. Polym. J.* **81**, 161–172 (2016).
39. Zheng, E. et al. Chemical polymerization of hydroxymethyl and chloromethyl functionalized PEDOT: PSS. *ACS Appl. Polym. Mater.* **1**, 3103–3114 (2019).
40. Yang, B. et al. A conductive PEDOT/alginate porous scaffold as a platform to modulate the biological behaviors of brown adipose-derived stem cells. *Biomater. Sci.* **8**, 3173–3185 (2020).
41. Andree, V. et al. Influence of drying methods on the physical properties of bacterial nanocellulose. *Mater. Res. Express* **8**, 025402 (2021).
42. Liu, T. et al. Surface modification with dopamine and heparin/poly-L-lysine nanoparticles provides a favorable release behavior for the healing of vascular stent lesions. *ACS Appl. Mater. Interfaces* **6**, 8729–8743 (2014).
43. Ivanko, I. et al. Tuning the photoluminescence and anisotropic structure of PEDOT. *J. Mater. Chem. C* **7**, 7013–7019 (2019).
44. Li, Z. et al. Inkjet printed disposable high-rate on-paper micro-supercapacitors. *Adv. Funct. Mater.* **32**, 2108773 (2021).
45. Li, Y. et al. Poly(3, 4-ethylenedioxythiophene): methylnaphthalene sulfonate formaldehyde condensate: the effect of work function and structural homogeneity on hole injection/extraction properties. *Adv. Energy Mater.* **7**, 1601499 (2016).
46. Feng, X. et al. Novel PEDOT dispersion by in-situ polymerization based on sulfated nanocellulose. *Chem. Eng. J.* **418**, 129533 (2021).
47. Liu, T. et al. Tailoring vertical phase distribution of quasi-two-dimensional perovskite films via surface modification of hole-transporting layer. *Nat. Commun.* **10**, 878 (2019).
48. Xin, X. et al. Freeze-drying and mechanical redispersion of aqueous PEDOT: PSS. *J. Appl. Polym. Sci.* **138**, 49774 (2020).
49. Tóth, J. et al. Separation of the first adsorbed layer from others and calculation of the BET compatible surface area from Type II isotherms. *J. Colloid Interface Sci.* **212**, 411–418 (1999).
50. Thommes, M. et al. Physisorption of gases, with special reference to the evaluation of surface area and pore size distribution (IUPAC Technical Report). *Pure Appl. Chem.* **87**, 1051–1069 (2015).
51. Ji, X. et al. All-in-one energy storage devices supported and interfacially cross-linked by gel polymeric electrolyte. *Energy Storage Mater.* **37**, 587–597 (2021).
52. Paluck, S. J. et al. Heparin-mimicking polymers: synthesis and biological applications. *Biomacromolecules* **17**, 3417–3440 (2016).
53. Li, Q. et al. A high-performance and flexible electrode film based on bacterial cellulose/polypyrrole/nitrogen-doped graphene for supercapacitors. *Carbohydr. Polym.* **311**, 120754 (2023).
54. Zhao, L. et al. Constructing mutual-philic electrode/non-liquid electrolyte interfaces in electrochemical energy storage systems: reasons, progress, and perspectives. *Energy Storage Mater.* **58**, 48–73 (2023).
55. Cho, K. W. et al. Soft bioelectronics based on nanomaterials. *Chem. Rev.* **122**, 5068–5143 (2021).
56. Song, X. et al. Self-anticoagulant nanocomposite spheres for the removal of bilirubin from whole blood: a step toward a wearable artificial liver. *Biomacromolecules* **21**, 1762–1775 (2020).
57. Nahain, A. A. et al. Anticoagulant heparin mimetics via RAFT polymerization. *Biomacromolecules* **21**, 1009–1021 (2019).
58. Ran, F. et al. A new approach for membrane modification based on electrochemically mediated living polymerization and self-assembly of N-tert-butyl amide- and β -cyclodextrin-involved macromolecules for blood purification. *Mater. Sci. Eng. C* **95**, 122–133 (2019).
59. Shih, C. C. et al. A rapid and green method for the fabrication of conductive hydrogels and their applications in stretchable supercapacitors. *J. Power Sources* **426**, 205–215 (2019).
60. Li, J. et al. Natively stretchable micro-supercapacitors based on a PEDOT: PSS hydrogel. *J. Mater. Chem. C* **9**, 1685–1692 (2021).
61. Zeng, J. et al. Highly stretchable, compressible and arbitrarily deformable all-hydrogel soft supercapacitors. *Chem. Eng. J.* **383**, 123098 (2020).
62. Zhang, C. et al. Highly flexible and transparent solid-state supercapacitors based on RuO₂/PEDOT: PSS conductive ultrathin films. *Nano Energy* **28**, 495–505 (2016).
63. Manjakkal, L. et al. A wearable supercapacitor based on conductive PEDOT: PSS-coated cloth and a sweat electrolyte. *Adv. Mater.* **32**, 1907254 (2020).
64. Sim, H. J. et al. Biomolecule based fiber supercapacitor for implantable device. *Nano Energy* **47**, 385–392 (2018).
65. Tahir, M. et al. Co-electrodeposited porous PEDOT-CNT micro-electrodes for integrated micro-supercapacitors with high energy density, high rate capability, and long cycling life. *Nanoscale* **11**, 7761–7770 (2019).
66. Yang, H. et al. Assembly of NiO/Ni(OH)₂/PEDOT nanocomposites on contra wires for fiber-shaped flexible asymmetric supercapacitors. *ACS Appl. Mater. Interfaces* **8**, 1774–1779 (2016).
67. Yu, M. et al. All-in-one membrane micro-supercapacitors for implantable devices. *J. Membr. Sci.* **687**, 122084 (2023).
68. Ma, Y. et al. Self-powered, one-stop, and multifunctional implantable triboelectric active sensor for real-time biomedical monitoring. *Nano Lett.* **16**, 6042–6051 (2016).
69. Zhao, Y. et al. Injectable fiber batteries for all-region power supply in vivo. *J. Mater. Chem. A* **9**, 1463–1470 (2021).
70. Wang, H. et al. Suppressing the self-discharge of supercapacitors by modifying separators with an ionic polyelectrolyte. *Adv. Mater. Interfaces* **5**, 1701547 (2018).
71. Zhang, Q. et al. The governing self-discharge processes in activated carbon fabric-based supercapacitors with different organic electrolytes. *Energy Environ. Sci.* **4**, 2152–2159 (2011).
72. Zhao, C. et al. Reduced self-discharge of supercapacitors using piezoelectric separators. *ACS Appl. Energy Mater.* **4**, 8070–8075 (2021).
73. Chae, J. S. et al. A durable high-energy implantable energy storage system with binder-free electrodes useable in body fluids. *J. Mater. Chem. A* **10**, 4611–4620 (2022).
74. Khan, S. et al. Bacterial cellulose-poly (3, 4-ethylenedioxythiophene)-poly (styrenesulfonate) composites for optoelectronic applications. *Carbohydr. Polym.* **127**, 86–93 (2015).
75. Eltayeb, N. E. et al. Preparation and properties of newly synthesized Polyaniline@Graphene oxide/Ag nanocomposite for highly selective sensor application. *J. Mater. Res. Technol.* **9**, 10459–10467 (2020).
76. Yang, Y. et al. Visualizing nucleation and growth process of vanadium-supramolecular nanoribbons self-assembled by rapid cooling method towards high-capacity vanadium nitride anode materials. *Adv. Energy Mater.* **12**, 2103158 (2022).
77. Liu, Y. et al. Energy storage mechanism of vanadium nitride via intercalating different atomic radius for expanding interplanar spacing. *Energy Environ. Mater.* **5**, 565–571 (2021).

78. Yang, L. et al. A robust mussel-inspired zwitterionic coating on biodegradable poly(L-lactide) stent with enhanced anticoagulant, anti-inflammatory, and anti-hyperplasia properties. *Chem. Eng. J.* **427**, 130910 (2022).
79. Wang, X. et al. Dual-site biomacromolecule doped poly (3, 4-ethylenedioxythiophene) for boosting both anticoagulant and electrochemical performances. *Adv. Healthc. Mater.* e2401134 <https://doi.org/10.1002/adhm.202401134> (2024).

Acknowledgements

This work was partly supported by the National Natural Science Foundation of China (51763014 and 52073133), the Key Talent Project Foundation of Gansu Province, a Joint fund between Shenyang National Laboratory for Materials Science and State Key Laboratory of Advanced Processing and Recycling of Nonferrous Metals (18LHPY002), and the Program for Hongliu Distinguished Young Scholars in Lanzhou University of Technology.

Author contributions

X.W. and F.R. conceived and designed the study. X.W. designed and performed all experiments. M.Y., M.K.H., and Y.Z. helped with electrochemical and hemocompatibility measurements. X.W., J.N., and M.Y. provided assistance in data analysis and revision. X.W. and F.R. wrote the manuscript. F.R. and Q.Z. provided financial support and research oversight. All authors contributed to the analysis and discussion of the data.

Competing interests

The authors declare no competing interests.

Additional information

Supplementary information The online version contains supplementary material available at <https://doi.org/10.1038/s41467-024-54862-2>.

Correspondence and requests for materials should be addressed to Fen Ran.

Peer review information *Nature Communications* thanks Hengchong Shi, and the other, anonymous, reviewer(s) for their contribution to the peer review of this work. A peer review file is available.

Reprints and permissions information is available at <http://www.nature.com/reprints>

Publisher's note Springer Nature remains neutral with regard to jurisdictional claims in published maps and institutional affiliations.

Open Access This article is licensed under a Creative Commons Attribution-NonCommercial-NoDerivatives 4.0 International License, which permits any non-commercial use, sharing, distribution and reproduction in any medium or format, as long as you give appropriate credit to the original author(s) and the source, provide a link to the Creative Commons licence, and indicate if you modified the licensed material. You do not have permission under this licence to share adapted material derived from this article or parts of it. The images or other third party material in this article are included in the article's Creative Commons licence, unless indicated otherwise in a credit line to the material. If material is not included in the article's Creative Commons licence and your intended use is not permitted by statutory regulation or exceeds the permitted use, you will need to obtain permission directly from the copyright holder. To view a copy of this licence, visit <http://creativecommons.org/licenses/by-nc-nd/4.0/>.

© The Author(s) 2024